CHAPTER 3

PROGRESS IN FULLY NONLINEAR POTENTIAL FLOW MODELING OF 3D EXTREME OCEAN WAVES

Stephan T. Grilli*

*Department of Ocean Engineering, University of Rhode Island
Narragansett, RI 02882, USA
grilli@oce.uri.edu*

Frédéric Dias[†]

*CMLA, ENS Cachan, CNRS, PRES UniverSud, 61 Av. President
Wilson, F-94230 Cachan, France*

Philippe Guyenne[‡]

*Department of Mathematical Sciences, University of Delaware, Newark
DE 19716, USA*

Christophe Fochesato[§]

*CMLA, ENS Cachan, CNRS, PRES UniverSud, 61 Av. President
Wilson, F-94230 Cachan, France*

François Enet[¶]

*Alkyon Hydraulic Consultancy and research, 8316PT Marknesse
The Netherlands*

This article reviews recent research progress by the authors and co-workers, in the application of three-dimensional (3D) Numerical Wave Tanks (NWT), based on Fully Nonlinear Potential Flow theory (FNPF), to the modeling of extreme, overturning, ocean waves and of their properties, in both deep and shallow water. Details of the model equations and numerical methods are presented. Applications are then presented for the shoaling and 3D overturning in shallow water of solitary waves over a sloping ridge, for the generation of extreme deep and intermediate water waves, often referred to as "rogue" waves, by directional energy focusing, for the generation of tsunamis by solid underwater landslides, and for the generation of surface waves by a moving pressure disturbance. In all cases, physical and numerical aspects are presented and properties of generated waves are discussed at the breaking point. Aspects of numerical methods influencing the accuracy and the efficiency of the NWT solution are detailed in the article. Specifically, the 3D-NWT equations are expressed in a mixed Eulerian-Lagrangian formulation (or pseudo-Lagrangian in one case) and solved based on a higher-order Boundary Element Method (BEM), for the spatial solution, and using explicit higher-order Taylor series expansions for the time integration. Direct and iterative solutions of the governing equations are discussed, as well as results of a recent application of the Fast Multipole Algorithm. Detailed aspects of the model such as the treatment of surface piercing solid boundaries are discussed as well.

1. Introduction

Over the last three decades, many studies have been carried out to achieve a better modeling and understanding of the generation of extreme waves in the deep ocean, as well as the propagation, shoaling, and breaking of ocean waves over a sloping nearshore topography. Such work was motivated by a variety of fundamental and practical ocean engineering problems. For instance, a description of the dynamics of breaking waves is necessary to explain the mechanisms of air–sea interactions, such as energy and momentum transfer from wind to water and from waves to currents, and the generation of turbulence in the upper ocean. The interaction and impact of extreme ocean waves (often referred to as rogue waves) with fixed or floating structures in deep water is thought to represent one of the highest hazard for the design of such structures. In nearshore areas, breaking wave induced currents are the driving mechanism for sediment transport, which leads to beach erosion and accretion, and also represent the design load for coastal structures used for shoreline and harbor protection. Despite significant progress, due to its complexity, the process of wave breaking has not

yet been fully explained. Reviews of wave breaking phenomena in shallow and deep water can be found in Refs. 1 and 2, respectively.

In this chapter, we report on our experience with three-dimensional (3D) numerical simulations aimed at very accurately describing the early stages of wave breaking induced by directional energy focusing in deep water and changes in topography in shallow water, namely the phenomenon of wave overturning. Additionally, we report on additional applications of the same modeling approach, to the generation of tsunamis by underwater landslides and the generation of waves by a moving free surface pressure disturbance representing the air cushion of a fast surface effect ship.

We concentrate on cases in which 3D effects are induced in the wave flow, and, at the final stages of wave overturning, we pay particular attention to large size plunging breakers which are characterized by the formation of a more prominent jet (rather than smaller size spilling breakers). Such large jets would create the strongest wave impact on ocean structures, as well as cause the larger disturbances in beach sediment. A high-order 3D numerical model, solving Fully Nonlinear Potential Flow (FNPF) equations is developed and used in this work. The potential flow approximation is justified for initially irrotational waves or flows starting from rest, considering the slow diffusion of vorticity from boundaries until the breaker jet touches down. In fact, comparisons of two-dimensional (2D) numerical results with laboratory experiments have consistently shown that FNPF theory accurately predicts the characteristics of wave overturning, in deep water (e.g., Refs. 3 and 4), as well as wave shoaling and overturning over slopes (e.g., Refs. 5 and 6). In the latter work, the model predicts the shape and kinematics of shoaling solitary waves over mild slopes, within 2% of experimental measurements in a precision wavetank, up to the breaking point. Other experiments showed that the shape of such overturning waves is then accurately modeled up to touch down.[7,8] Beyond touch down of the breaker jet, strong vorticity and energy dissipation occur and a full Navier-Stokes (NS) model must be used. Lin and Liu,[9] Chen et al.[10] and Christensen and Deigaard,[11] for instance, studied the breaking and post-breaking of solitary waves using a 2D-NS model. The latter authors also calculated 3D turbulent fields using a LES model and Lubin[12] similarly performed 3D LES simulations of plunging breaking waves. Guignard et al.[13] and Lachaume et al.[14] proposed a coupled model that combines both the accuracy and efficiency of a 2D-FNPF model, used during the shoaling and overturning phases of wave propagation, and a 2D-NS modeling of the surfzone.

Due to computer limitations, detailed numerical studies of wave breaking with FNPF models have initially focused on 2D problems. In this respect, significant contributions in the numerical simulation of steep fully nonlinear waves were made by Longuet-Higgins and Cokelet,[15] who first proposed a mixed Eulerian–Lagrangian (MEL) approach for the time updating, combined with a Boundary Integral Equation (BIE) formulation, in a deep water space-periodic domain. Their computations were able to reproduce overturning waves by specifying a localized surface pressure. Similar methods were adopted in subsequent works, notably, by Vinje and Brevig[16] and Baker et al.,[17] who considered the case of finite depth. Results obtained by New et al.[18,19] for plunging waves over constant depth, greatly contributed to our understanding of breaking wave kinematics. These authors carried out high-resolution computations for various types of breakers and analyzed in detail the overturning motions, by following fluid particle trajectories in the space, velocity, and acceleration planes. More recent 2D-FNPF models can accommodate both arbitrary waves and complex bottom topography, as well as surface-piercing moving boundaries such as wavemakers. These models are directly implemented in a physical space region, where incident waves can be generated at one extremity and reflected, absorbed or radiated at the other extremity (e.g., Refs. 20–23). For these reasons, they are often referred to as Numerical Wave Tanks (NWT).

A comparatively smaller number of works have addressed, essentially non-breaking, 3D-FNPF wave simulations, due to the more difficult geometric representation as well as the more demanding computational problems (e.g., Refs. 24, 25, 28–33). In particular, the problem of strongly nonlinear waves requires very accurate and stable numerical methods, and this consequently leads to an increase of the computational cost. Xü and Yue[34] and Xue et al.[35] calculated 3D overturning waves in a doubly periodic domain with infinite depth (i.e. only the free surface is discretized). They used a quadratic Boundary Element Method (BEM) to solve the equations in a MEL formulation. As in Ref. 15, the initial conditions were progressive Stokes waves and a localized surface pressure was applied to make waves break. These authors performed a detailed analysis of the kinematics of plunging waves and quantified the three-dimensional effects on the flow,[26,27] developed a similar method, for a non-periodic domain with finite depth. They were also able to produce the initial stages of wave overturning over a bottom obstacle. More recently, Grilli et al.[36] proposed an accurate 3D NWT model, for the description of strongly nonlinear wave generation and propagation over complex bottom topography. This NWT is based

on a MEL explicit time stepping and a high-order BEM with third-order spatial discretization, ensuring local continuity of the inter-element slopes. Arbitrary waves can be generated in this NWT and, if needed, absorbing conditions can be specified on lateral boundaries. Although an application to the shoaling of a solitary wave up to overturning was shown, this initial paper focused more on the derivation and validation of the numerical model and methods rather than on the physical implications of results. Other applications and extensions of this NWT to other nonlinear wave processes were done for the modelling of: (i) wave impact on a vertical wall;[37] (ii) freak wave generation due to directional wave focusing;[38–40] (iii) tsunami generation by submarine mass failure;[41–43] (iv) the generation of waves by a moving surface pressure disturbance;[44–46] and (v) the simulation of co-seismic tsunami generation by a specified bottom motion.[47] The reader interested in boundary integral methods, especially in applications to 3D free surface flows, is also referred to Ref. 48.

In this chapter, we first detail equations and numerical methods for the 3D-FNPF NWT model initially developed by Ref. 36, and subsequently extended by Refs. 38, 41, 45, 50 and 49, concentrating on the different types of boundary conditions, free surface updating, boundary representation, and fast equation solver. We then present a number of typical applications of the model to the breaking of solitary waves over a sloping ridge, extreme overturning waves created by directional energy focusing using a wavemaker, landslide tsunami generation, and surface wave generation by a moving disturbance. Due to the complexity of the problem and the high computational cost, our studies of 3D breakers are typically restricted to fairly small spatial domains. Beside wave shape, various results are presented for the velocity and acceleration fields before and during wave overturning, both on the free surface and within the flow. We stress that no smoothing of the solution is required, e.g., to suppress spurious waves at any time in the computations, as experienced in most of the other proposed models.

2. Mathematical Formulation

2.1. *Governing equations and boundary conditions*

We assume an incompressible inviscid fluid, with irrotational motion described by the velocity potential $\phi(\boldsymbol{x}, t)$, in a Cartesian coordinate system $\boldsymbol{x} = (x, y, z)$ (with z the vertical upward direction and $z = 0$ at the undisturbed free surface).
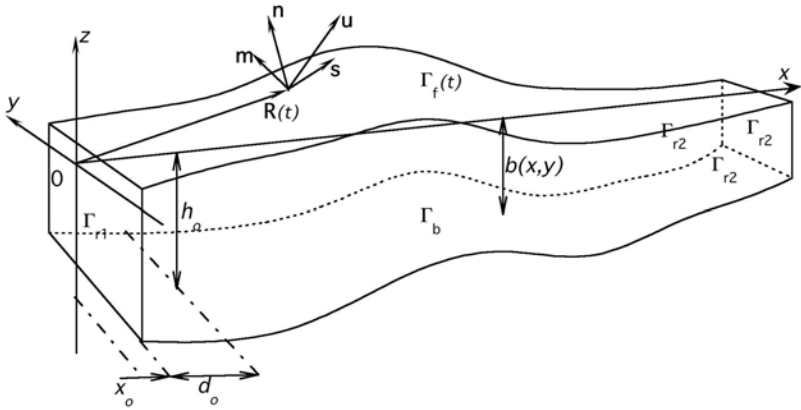
Fig. 1. Sketch of typical computational domain for 3D-BEM solution of FNPF equations. Tangential vectors at point $\boldsymbol{R}(t)$ on the free surface $\Gamma_f(t)$ are defined as $(\boldsymbol{s}, \boldsymbol{m})$ and outward normal vector as $\boldsymbol{n}$.

The fluid velocity is thus defined as $\boldsymbol{u} = \boldsymbol{\nabla}\phi = (u, v, w)$ and mass conservation is Laplace's equation for the potential, which in the fluid domain $\Omega(t)$ with boundary $\Gamma(t)$ reads (Fig. 1),

$$\nabla^2 \phi = 0\,. \tag{2.1}$$

Applying Green's second identity, Eq. (2.1) transforms into the BIE,

$$\alpha(\boldsymbol{x}_l)\phi(\boldsymbol{x}_l) = \int_\Gamma \left\{ \frac{\partial \phi}{\partial n}(\boldsymbol{x})G(\boldsymbol{x}, \boldsymbol{x}_l) - \phi(\boldsymbol{x})\frac{\partial G}{\partial n}(\boldsymbol{x}, \boldsymbol{x}_l) \right\} d\Gamma \tag{2.2}$$

where the field point $\boldsymbol{x}_l$ and the source point $\boldsymbol{x}$ are both on the boundary, $\alpha(\boldsymbol{x}_l) = \frac{1}{4\pi}\theta_l$, with θ_l the exterior solid angle at point $\boldsymbol{x}_l$, and the three-dimensional (3D) free-space Green's function is defined as,

$$G(\boldsymbol{x}, \boldsymbol{x}_l) = \frac{1}{4\pi r} \quad \text{with} \quad \frac{\partial G}{\partial n}(\boldsymbol{x}, \boldsymbol{x}_l) = -\frac{1}{4\pi}\frac{\boldsymbol{r} \cdot \boldsymbol{n}}{r^3} \tag{2.3}$$

where $r = |\boldsymbol{r}| = |\boldsymbol{x} - \boldsymbol{x}_l|$ and $\boldsymbol{n}$ is the outward unit vector normal to the boundary at point $\boldsymbol{x}$.

The boundary is divided into various parts with different boundary conditions (Fig. 1). On the free surface $\Gamma_f(t)$, ϕ satisfies the nonlinear kinematic and dynamic boundary conditions, which in the MEL formulation

read,

$$\frac{\mathrm{D}\boldsymbol{R}}{\mathrm{D}t} = \boldsymbol{u} \tag{2.4}$$

$$\frac{\mathrm{D}\phi}{\mathrm{D}t} = -gz + \tfrac{1}{2}\boldsymbol{\nabla}\phi \cdot \boldsymbol{\nabla}\phi - \frac{p_a}{\rho} \tag{2.5}$$

respectively, with $\boldsymbol{R}$ the position vector of a fluid particle on the free surface, g the gravitational acceleration, p_a the atmospheric pressure, ρ the fluid density and $\mathrm{D}/\mathrm{D}t = \partial/\partial t + \boldsymbol{\nabla}\phi \cdot \boldsymbol{\nabla}$ the Lagrangian (or material) time derivative. Effects of surface tension are neglected considering the large scale waves modeled here (however, this could be easily added to Eq. (2.5)).

In earlier applications of the model, waves have been generated in various ways: (i) by directly specifying wave elevation and potential (such as a solitary wave; e.g., Ref. 51) on the free surface at $t = 0$;[36,37,52,53] (ii) by simulating a (solid) wavemaker motion at the 'open sea' boundary side of the model Γ_{r1};[38–40] (iii) by specifying the motion of a solid underwater landslide on the bottom boundary Γ_b;[41–43] or (iv) by a moving pressure disturbance on the free surface.[44–46,54]

Over moving boundaries such as wavemakers (or landslides), both the boundary geometry $\boldsymbol{x}_p(t)$ and normal fluid velocity are specified as,

$$\overline{\boldsymbol{x}} = \boldsymbol{x}_p \quad \text{and} \quad \overline{\frac{\partial\phi}{\partial n}} = \boldsymbol{u}_p \cdot \boldsymbol{n} \tag{2.6}$$

where overbars denote specified values and $\boldsymbol{u}_p(\boldsymbol{x}_p, t)$ is the boundary velocity.

In all cases, one (or two in case (iv)) open boundary conditions can be specified on some vertical sections $\Gamma_{r2}(t)$, of the model boundary. Following,[38,41] the open boundary is modeled as a pressure sensitive 'snake' flap- or piston-type absorbing wavemaker. For a piston-type boundary in depth h_o, for instance, the piston normal velocity is specified as,

$$\overline{\frac{\partial\phi}{\partial n}} = u_{ap}(\sigma, t) \qquad \text{on } \Gamma_{r2}(t), \text{ with,} \tag{2.7}$$

$$u_{ap}(\sigma, t) = \frac{1}{\rho h_o \sqrt{gh_o}} \int_{-h_o}^{\eta_{ap}(\sigma,t)} p_D(\sigma, z, t)\,\mathrm{d}z \tag{2.8}$$

calculated at the curvilinear abscissa σ, horizontally measured along the piston boundary, where η_{ap} is the surface elevation at the piston location and $p_D = -\rho_w\{\frac{\partial\phi}{\partial t} + \frac{1}{2}\nabla\phi \cdot \nabla\phi\}$ denotes the dynamic pressure. The integral in Eq. (2.8) represents the horizontal hydrodynamic force $F_D(\sigma, t)$ acting

on the piston at time t, as a function of σ. For 2D problems, Grilli and Horrillo[23] showed that this type of boundary condition absorbs well energy from long incident waves. Shorter waves, however, will be reflected to a greater extent by the boundary, but can directly be damped on the free surface using an 'Absorbing Beach' (AB). Such a pressure always works against the waves and hence is equivalent to an energy dissipation over time. For 2D problems, Grilli and Horrillo[23] implemented the AB over a section of the free surface by specifying the pressure in the dynamic boundary condition Eq. (2.5) such as to be opposite and proportional to the normal fluid velocity,

$$p_a = \nu(\boldsymbol{x}, t) \frac{\partial \phi}{\partial n}(\eta(\boldsymbol{x}, t)) \qquad (2.9)$$

in which ν, the AB absorption function, is smoothly varied along the AB and η refers to nodes on the free surface of elevation η. This approach was extended by Grilli et al.[55] to model the effect of energy dissipation due to bottom friction on the shoaling of 2D periodic waves. In this case, the coefficient $\nu(\boldsymbol{x}, t)$ was found at each time step by expressing a balance between the time averaged energy dissipation on the bottom and the free surface pressure. In some earlier applications of the 3D model,[44–46] a similar AB was specified over an area of the free surface to damp shorter waves, in combination with the absorbing wavemaker boundary. Note, recently, Dias et al.[56] derived new free surface boundary conditions to account for energy dissipation due to viscosity in potential flow equations. In these equations, a correction term is added to both the kinematic and dynamic boundary conditions, Eqs. (2.4) and (2.5), respectively. It should be of interest to implement this new set of equations in the NWT.

Except in case (iii), a no-flow condition is specified on the bottom Γ_b and other fixed parts of the boundary referred to as Γ_{r2} as,

$$\overline{\frac{\partial \phi}{\partial n}} = 0 \,. \qquad (2.10)$$

2.2. Internal velocity and acceleration

Once the BIE Eq. (2.2) is solved, the solution within the domain can be evaluated from the boundary values. Using Eq. (2.2), the internal velocity is given by,

$$\boldsymbol{u}(\boldsymbol{x}_i) = \boldsymbol{\nabla}\phi(\boldsymbol{x}_i) = \int_\Gamma \left[\frac{\partial \phi}{\partial n}(\boldsymbol{x})\boldsymbol{Q}(\boldsymbol{x}, \boldsymbol{x}_i) - \phi(\boldsymbol{x})\frac{\partial \boldsymbol{Q}}{\partial n}(\boldsymbol{x}, \boldsymbol{x}_i) \right] \mathrm{d}\Gamma \qquad (2.11)$$

with,

$$\boldsymbol{Q}(\boldsymbol{x}, \boldsymbol{x}_i) = \frac{1}{4\pi r^3}\boldsymbol{r}\,, \quad \frac{\partial \boldsymbol{Q}}{\partial n}(\boldsymbol{x}, \boldsymbol{x}_i) = \frac{1}{4\pi r^3}\left[\boldsymbol{n} - 3(\boldsymbol{r}\cdot\boldsymbol{n})\frac{\boldsymbol{r}}{r^2}\right] \qquad (2.12)$$

and r denoting the distance from the boundary point $\boldsymbol{x}$ to the interior point $\boldsymbol{x}_i$. Note that the coefficient $\alpha(\boldsymbol{x}_i)$ is unity for interior points.

Similarly, we express the internal Lagrangian acceleration as,

$$\frac{\mathrm{D}\boldsymbol{u}}{\mathrm{D}t} = \frac{\mathrm{D}}{\mathrm{D}t}\boldsymbol{\nabla}\phi = \frac{\partial}{\partial t}\boldsymbol{\nabla}\phi + (\boldsymbol{\nabla}\phi\cdot\boldsymbol{\nabla})\boldsymbol{\nabla}\phi \qquad (2.13)$$

where the first term on the right-hand side, corresponding to the local acceleration, is given by,

$$\boldsymbol{\nabla}\frac{\partial\phi}{\partial t}(\boldsymbol{x}_i) = \int_\Gamma \left[\frac{\partial^2\phi}{\partial t\partial n}(\boldsymbol{x})\boldsymbol{Q}(\boldsymbol{x}, \boldsymbol{x}_i) - \frac{\partial\phi}{\partial t}(\boldsymbol{x})\frac{\partial\boldsymbol{Q}}{\partial n}(\boldsymbol{x}, \boldsymbol{x}_i)\right]\mathrm{d}\Gamma \qquad (2.14)$$

and the second term is computed using Eq. (2.11) and differentiating $\boldsymbol{\nabla}\phi$. This requires calculating the spatial derivatives of all components of $\boldsymbol{Q}$ and $\partial\boldsymbol{Q}/\partial n$ as, (note, the index summation convention does not apply for the two following equations)

$$\frac{\partial Q_k}{\partial x_j} = \begin{cases} \frac{3}{4\pi r^5}r_k r_j\,, & k \neq j \\ \frac{1}{4\pi r^3}\left(\frac{3}{r^2}r_k^2 - 1\right), & k = j \end{cases} \qquad (2.15)$$

$$\frac{\partial}{\partial x_j}\left(\frac{\partial Q_k}{\partial n}\right) = \begin{cases} \frac{3}{4\pi r^5}\left[r_j n_k + r_k n_j - \frac{5}{r^2}(\boldsymbol{r}\cdot\boldsymbol{n})r_k r_j\right], & k \neq j \\ \frac{3}{4\pi r^5}\left[\boldsymbol{r}\cdot\boldsymbol{n} + 2r_k n_k - \frac{5}{r^2}(\boldsymbol{r}\cdot\boldsymbol{n})r_k^2\right], & k = j\,, \end{cases} \qquad (2.16)$$

where k, j refer to the spatial dimensions and r_k stands for the k-th component of $\boldsymbol{r}$.

The boundary quantities $\partial\phi/\partial t$ and $\partial^2\phi/\partial t\partial n$ in Eq.(2.14) also satisfy a BIE similar to Eq. (2.2), for ϕ and $\partial\phi/\partial n$. In fact, this second BIE is solved at each time step to compute these fields, which are necessary to perform the second-order time updating of free surface nodes; this is detailed in Section 3.2.

2.3. *Boundary velocity and acceleration*

As will be detailed in Section 3.2, particle velocity $\boldsymbol{u}$ and acceleration $\mathrm{D}\boldsymbol{u}/\mathrm{D}t$ are used to perform the second-order Lagrangian time updating of collocation nodes on the free surface. Similar terms are also needed for

expressing boundary conditions on other moving or deforming parts of the boundary, such as wavemakers, open boundaries, or underwater landslides.

At boundary nodes, geometry, field variables and their derivatives are expressed in a local curvilinear coordinate system $(\boldsymbol{s}, \boldsymbol{m}, \boldsymbol{n})$ (Fig. 2) defined within a single reference element, which for practical reasons is different from that of the BEM discretization that will be detailed in Section 3.1. Thus, at each collocation point $\boldsymbol{x}_l$ on the boundary, the unit tangential vectors are defined as

$$\boldsymbol{s} = \frac{1}{h_1}\frac{\partial \boldsymbol{x}_l}{\partial \xi} \quad \text{and} \quad \boldsymbol{m} = \frac{1}{h_2}\frac{\partial \boldsymbol{x}_l}{\partial \eta} \tag{2.17}$$

where

$$h_1 = \left|\frac{\partial \boldsymbol{x}_l}{\partial \xi}\right|, \quad h_2 = \left|\frac{\partial \boldsymbol{x}_l}{\partial \eta}\right| \tag{2.18}$$

and $-1 \leq (\xi, \eta) \leq 1$ denote the intrinsic coordinates of the reference element (this aspect will also be detailed later). A third unit vector in the normal direction is then defined as $\boldsymbol{n} = (\boldsymbol{s} \times \boldsymbol{m})/\sin \widehat{(\boldsymbol{s}, \boldsymbol{m})}$.

For the initial typically orthogonal discretization in the model, the local coordinate system $(\boldsymbol{s}, \boldsymbol{m}, \boldsymbol{n})$ is also orthogonal and we simply have $\boldsymbol{n} = \boldsymbol{s} \times \boldsymbol{m}$. Unlike initially assumed,[36] however, the orthogonality of $\boldsymbol{s}$ and $\boldsymbol{m}$ does not strictly hold when the boundary elements are distorted, such as in regions of large surface deformations. Fochesato et al.[50] extended the expressions of tangential derivatives to the general case when $\boldsymbol{s}$ and $\boldsymbol{m}$ are not orthogonal; this is summarized below.
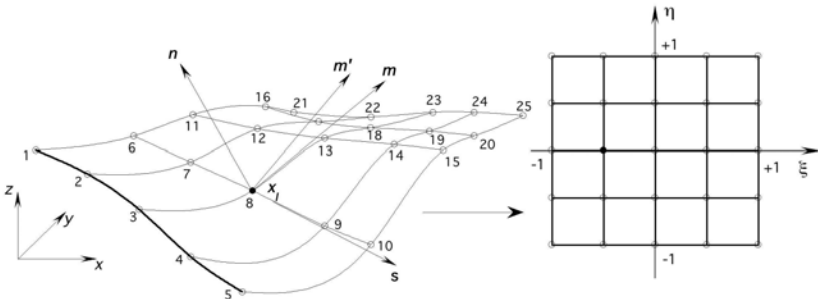

Fig. 2.   Sketch of local interpolation by fourth-order two-dimensional sliding polynomial element of (ξ, η), for calculating tangential derivatives in orthogonal axes $(\boldsymbol{s}, \boldsymbol{m}', \boldsymbol{n})$ at collocation point $\boldsymbol{x}_l$ on the boundary.

Using $\boldsymbol{s}$ and $\boldsymbol{m}$ in Eq. (2.17), one can define a new unit tangential vector as (Fig. 2)

$$\boldsymbol{m}' = \frac{1}{\sqrt{1-\kappa^2}}\boldsymbol{m} - \frac{\kappa}{\sqrt{1-\kappa^2}}\boldsymbol{s} \qquad (2.19)$$

so that $\boldsymbol{s}$ and $\boldsymbol{m}'$ are orthogonal (i.e., $\boldsymbol{s}\cdot\boldsymbol{m}' = 0$), with $\kappa = \boldsymbol{s}\cdot\boldsymbol{m} = \cos\widehat{(\boldsymbol{s},\boldsymbol{m})}$ (Fig. 2). This implies that $-1 < \kappa < 1$. The unit normal vector now takes the form

$$\boldsymbol{n} = \boldsymbol{s} \times \boldsymbol{m}' = \frac{1}{\sqrt{1-\kappa^2}}\boldsymbol{s} \times \boldsymbol{m} \qquad (2.20)$$

(which does yield $\boldsymbol{m}' = \boldsymbol{m}$ and $\boldsymbol{s}\cdot\boldsymbol{m} = 0$ only when $\kappa = 0$). For clarity, let us introduce the following notations

$$(\ )_s \equiv \frac{\partial}{\partial s} = \frac{1}{h_1}\frac{\partial}{\partial\xi}, \quad (\ )_m \equiv \frac{\partial}{\partial m} = \frac{1}{h_2}\frac{\partial}{\partial\eta}, \quad (\ )_n \equiv \frac{\partial}{\partial n} \qquad (2.21)$$

and

$$(\ )_{ss} \equiv \frac{1}{h_1^2}\frac{\partial^2}{\partial\xi^2}, \quad (\ )_{sm} \equiv \frac{1}{h_1 h_2}\frac{\partial^2}{\partial\xi\partial\eta}, \quad (\ )_{mm} \equiv \frac{1}{h_2^2}\frac{\partial^2}{\partial\eta^2}. \qquad (2.22)$$

In the orthonormal coordinate system $(\boldsymbol{s},\boldsymbol{m}',\boldsymbol{n})$, the particle velocity on the boundary is expressed as

$$\boldsymbol{u} = \boldsymbol{\nabla}\phi = \phi_s\boldsymbol{s} + \phi_{m'}\boldsymbol{m}' + \phi_n\boldsymbol{n} \qquad (2.23)$$

where ϕ denotes the velocity potential. In the general coordinate system $(\boldsymbol{s},\boldsymbol{m},\boldsymbol{n})$, this equation thus becomes

$$\boldsymbol{u} = \frac{1}{1-\kappa^2}(\phi_s - \kappa\phi_m)\boldsymbol{s} + \frac{1}{1-\kappa^2}(\phi_m - \kappa\phi_s)\boldsymbol{m} + \phi_n\boldsymbol{n} \qquad (2.24)$$

after using Eq. (2.19) and the fact that

$$\phi_{m'} = \frac{1}{\sqrt{1-\kappa^2}}\phi_m - \frac{\kappa}{\sqrt{1-\kappa^2}}\phi_s. \qquad (2.25)$$

Laplace's equation $\boldsymbol{\nabla}^2\phi = 0$ can be similarly expressed on the boundary, as well as particle accelerations (by applying the material derivative to Eq. (2.24)), which are both required to calculate second-order terms in the time updating method (see Section 3.2). These expressions are given in Appendix A.1.

3. Numerical Methods

Many different numerical methods have been proposed for solving FNPF equations for water waves in 2D or 3D (see, e.g., Ref. 57 for a recent review). Here we solve FNPF equations using the BIE formulation outlined above, which was initially implemented[36] in this 3D model, based on initial 3D-BEM modeling of linear waves[58] and as an extension of earlier 2D-FNPF models.[20,22,23,59,60] The model benefits from recent improvements in the numerical formulations and solution.[49,50] Numerical methods are briefly summarized below and detailed in the following subsections.

The model consists in a time stepping algorithm in which the position vector and velocity potential on the free surface are updated, based on second-order Taylor series expansions. At each time step, the BIE Eq. (2.2) is expressed for N_Γ collocation nodes, defining the domain boundary Γ, and solved with a BEM, in which boundary elements are specified in between nodes, to locally interpolate both the boundary geometry and field variables, using bi-cubic polynomial shape functions. A local change of variables is defined to express the BIE integrals on a single curvilinear reference element, and compute these using a Gauss-Legendre quadrature and other appropriate techniques removing the weak singularities of the Green's function (based on polar coordinate transformations). The number of discretization nodes yields the assembling phase of the system matrix, resulting in an algebraic system of equations. The rigid mode technique is applied to directly compute external angles α_l and diagonal terms in the algebraic system matrix, which would normally require evaluating strongly singular integrals involving the normal derivative of the Green's function. Multiple nodes are specified on domain edges and corners, in order to easily express different normal directions on different sides of the boundary. Additional equations derived for enforcing continuity of the potential at these nodes also lead to modifications of the algebraic system matrix. The velocity potential (or its normal derivative depending on the boundary condition) is obtained as a solution of the linear system of equations. Since the system matrix is typically fully populated and non-symmetric, the method has, at best, a computational complexity of $O(N_\Gamma^2)$, when using an iterative, optimized conjugate gradient method such as GMRES (see, e.g., Refs. 34 and 35). Thus the spatial solution at each time step is of the same complexity as the numerical cost of assembling of the system matrix. The Fast Multipole Algorithm (FMA) is implemented in the model to reduce this complexity to $O(N_\Gamma \log N_\Gamma)$.

3.1. *Boundary discretization*

A BEM is used to solve the BIE (2.2) for ϕ, and due to the second-order time stepping, a similar equation for $\frac{\partial \phi}{\partial t}$. Thus, the boundary is discretized into N_Γ collocation nodes and M_Γ high-order boundary elements are defined for the local interpolation of both the geometry and field variables in between these nodes. While standard isoparametric elements based on polynomial shape functions can provide a high-order approximation within their area of definition, they only offer $\mathcal{C}^0$ continuity at nodes located in between elements (e.g., Ref. 61). In their 2D work, Grilli et al.[20,22] showed that such discontinuities in slope and curvature can be a source of inaccuracy that, through time updating, may trigger sawtooth instabilities in the model near the crest of steep waves or within overturning jets. These authors showed that a robust treatment requires defining elements, which are both of high-order within their area of definition and at least locally $\mathcal{C}^2$ continuous at their edges. Among various types of approximations, they proposed using so-called middle-interval-interpolation (MII) elements, which in 2D are 4-nodes cubic isoparametric elements, in which only the interval between the middle two nodes is used for the interpolation. In the initially developed 3D model,[36] we used an extension of the MII by defining boundary elements that are 4×4-node quadrilaterals associated with bi-cubic shape functions. Only one out of the nine sub-quadrilaterals so defined is used for the interpolation, typically the central one, but any other is used for elements located at the intersections between different boundary sections, depending on the location (Fig. 3).

Specifically, the boundary geometry and field variables (denoted hereafter by $u \equiv \phi$ or $\frac{\partial \phi}{\partial t}$ and $q \equiv \frac{\partial \phi}{\partial n}$ or $\frac{\partial^2 \phi}{\partial t \partial n}$ for simplicity) are represented within each MII element using shape functions N_j as,

$$\boldsymbol{x}(\xi, \eta) = N_j(\xi, \eta)\, \boldsymbol{x}_j^k \tag{3.1}$$

$$u(\xi, \eta) = N_j(\xi, \eta)\, u_j^k \quad \text{and} \quad q(\xi, \eta) = N_j(\xi, \eta)\, q_j^k \tag{3.2}$$

where $\boldsymbol{x}_j^k$, u_j^k and q_j^k, are nodal values of geometry and field variables, respectively, for $j = 1, \ldots, m$, locally numbered nodes within each element Γ_e^k, $k = 1, \ldots, M_\Gamma$, and the summation convention is applied to repeated subscripts. Here, shape functions are analytically defined as bi-cubic polynomials over a single reference element $\Gamma_{\xi,\eta}$, to which the M_Γ "Cartesian" elements of arbitrary shape are transformed by a curvilinear change of variables, defined by the Jacobian matrix $\mathbf{J}^k$. The intrinsic coordinates on the

reference element are denoted by $(\xi, \eta) \in [-1, 1]$. The shape function polynomial coefficients are simply found analytically by requiring that $u(\xi, \eta)$ take the value u_i^k at node $\boldsymbol{x}_i^k$, that is in Eq. (3.2),

$$u(\xi(\boldsymbol{x}_i^k), \eta(\boldsymbol{x}_i^k)) = N_j(\xi_i, \eta_i)\, u_j^k = u_i^k\,.$$

Hence, for the i-th node of an m-node reference element, shape functions must satisfy,

$$N_j(\xi_i, \eta_i) = \delta_{ij} \quad \text{with} \quad i, j = 1, \ldots, m \ \text{ on } \Gamma_{\xi, \eta} \tag{3.3}$$

and δ_{ij} the Kronecker symbol.

We further define the shape functions as the product of two one-dimensional cubic shape functions $N_c'(\mu)$, with $c = 1, \ldots, 4$ and $\mu \in [-1, 1]$, i.e.

$$N_j(\xi, \eta) = N_{b(j)}'(\mu(\xi, \xi_o))\, N_{d(j)}'(\mu(\eta, \eta_o)) \tag{3.4}$$

with b and $d = 1, \ldots, 4$; $j = 4\,(d - 1) + b$, for which the property (3.3) implies,

$$N_c'(\mu_i) = \delta_{ic} \quad \text{with} \quad \mu_i = (2i - 5)/3 \tag{3.5}$$

for $i = 1, \ldots, 4$. Hence, solving Eq. (3.5) we find

$$N_1'(\mu) = \frac{1}{16}\,(1 - \mu)\,(9\mu^2 - 1) \;\; ; \;\; N_2'(\mu) = \frac{9}{16}\,(1 - \mu^2)\,(1 - 3\mu)$$

$$N_3'(\mu) = \frac{9}{16}\,(1 - \mu^2)\,(1 + 3\mu) \;\; ; \;\; N_4'(\mu) = \frac{1}{16}\,(1 + \mu)\,(9\mu^2 - 1)\,. \tag{3.6}$$

For the MII method, the additional transformation from μ to the intrinsic coordinates (ξ, η) on the reference element is formally expressed as,

$$\mu(\chi, \chi_o) = \chi_o + \frac{1}{3}\,(1 + \chi) \tag{3.7}$$

with $\chi = \xi$ or η, and $\chi_o = \xi_o$ or $\eta_o = -1, -1/3$ or $1/3$, depending on which of the 9 quadrilaterals defined by the $m = 16$ nodes is selected as a function of the location of the Cartesian element with respect to intersections between various parts of the boundary (Fig. 3).

Discretized BIEs

Integrals in Eq. (2.2) are transformed into a sum of integrals over the boundary elements Γ_e^k, $k = 1, \ldots, M_\Gamma$. Each of these integrals is calculated within the reference element $\Gamma_{\xi, \eta}$ by applying the curvilinear change of variables discussed above: $[\boldsymbol{x} \to (\xi, \eta)]$, for which the Jacobian matrix is
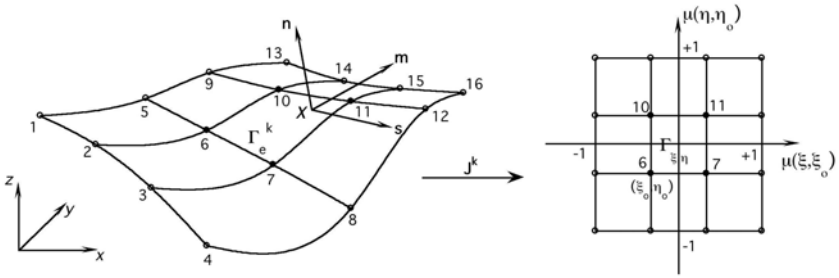
Fig. 3. Sketch of 16-node cubic 3D-MII Cartesian element Γ_e^k and corresponding reference element $\Gamma_{\xi,\eta}$. Quadrilateral element nodes are indicated by symbols ($\bullet$), and additional nodes by symbols ($\circ$). The curvilinear coordinate system (s, m, n) has been marked at point r of the element. (ξ_o, η_o) marks the bottom left node of the quadrilateral, transformed as part of the reference element by Jacobian $\mathbf{J}^k$.

obtained as follows. Using Eqs. (3.2) and (3.3), two tangential vectors are defined at arbitrary boundary point $\boldsymbol{x}(\xi, \eta)$ as,

$$\frac{\partial \boldsymbol{x}}{\partial \xi} = \frac{\partial N_j(\xi, \eta)}{\partial \xi} \, \boldsymbol{x}_j^k = \left\{ \frac{\partial N'_{b(j)}(\mu(\xi, \xi_o))}{\partial \mu} \, N'_{d(j)}(\mu(\eta, \eta_o)) \, \frac{\partial \mu}{\partial \xi} \right\} \boldsymbol{x}_j^k$$

$$\frac{\partial \boldsymbol{x}}{\partial \eta} = \frac{\partial N_j(\xi, \eta)}{\partial \eta} \, \boldsymbol{x}_j^k = \left\{ N'_{b(j)}(\mu(\xi, \xi_o)) \, \frac{\partial N'_{d(j)}(\mu(\eta, \eta_o))}{\partial \mu} \, \frac{\partial \mu}{\partial \eta} \right\} \boldsymbol{x}_j^k$$

$$(3.8)$$

with $j = 1, \ldots, m$ on Γ_e^k ($k = 1, \ldots, M_\Gamma$) and, by applying Eq. (3.7), $\frac{\partial \mu}{\partial \xi} = \frac{\partial \mu}{\partial \eta} = 1/3$. The corresponding tangential unit vectors $\boldsymbol{s}$ and $\boldsymbol{m}$ are further defined similar to Eqs. (2.17) and (2.18) for nodal points. As discussed before, these vectors are in general non-orthogonal. A local normal vector is defined based on these as,

$$\frac{\partial \boldsymbol{x}}{\partial \zeta} = \frac{\partial \boldsymbol{x}}{\partial \xi} \times \frac{\partial \boldsymbol{x}}{\partial \eta} \tag{3.9}$$

where the corresponding unit normal vector is thus defined as,

$$\boldsymbol{n}(\xi, \eta) = \frac{1}{h_1 \, h_2} \frac{\partial \boldsymbol{x}}{\partial \zeta} \qquad \text{with} \qquad \left| \frac{\partial \boldsymbol{x}}{\partial \zeta} \right| = h_1 \, h_2 \,. \tag{3.10}$$

Vector $\boldsymbol{n}$ will be pointing in the outward direction with respect to the domain if vectors $(\boldsymbol{s}, \boldsymbol{m})$ are such that their cross product is outward oriented (this is only a matter of definition of the considered element nodes numbering).

The Jacobian matrix is then defined as,

$$\mathbf{J}^k = \left\{ \frac{\partial \boldsymbol{x}}{\partial \xi}, \frac{\partial \boldsymbol{x}}{\partial \eta}, \boldsymbol{n} \right\}^T$$

and the determinant of the Jacobian matrix, to be used in boundary integrals for the k-th element is thus given by

$$| \mathbf{J}^k(\xi, \eta) | = h_1 h_2 \qquad \text{for } k = 1, \ldots, M_\Gamma \text{ on } \Gamma \qquad (3.11)$$

which can be analytically calculated at any point of a given element by using Eqs. (3.8) with the definitions Eqs. (3.6) of shape functions.

After elementary transformation, the discretized expressions of the integrals in Eq. (2.2) are obtained as,

$$\int_{\Gamma(\boldsymbol{x})} \frac{\partial \phi}{\partial n} G_l \, d\Gamma = \sum_{j=1}^{N_\Gamma} \left\{ \sum_{k=1}^{M_\Gamma} \int_{\Gamma_{\xi,\eta}} N_j(\xi, \eta) G(\boldsymbol{x}(\xi, \eta), \boldsymbol{x}_l) \mid \mathbf{J}^k(\xi, \eta) \mid d\xi d\eta \right\}$$

$$\frac{\partial \phi}{\partial n}(\boldsymbol{x}_j) = \sum_{j=1}^{N_\Gamma} \left\{ \sum_{k=1}^{M_\Gamma} D_{lj}^k \right\} \frac{\partial \phi_j}{\partial n} = \sum_{j=1}^{N_\Gamma} K_{lj}^d \frac{\partial \phi_j}{\partial n} \qquad (3.12)$$

$$\int_{\Gamma(\boldsymbol{x})} \phi \frac{\partial G_l}{\partial n} \, d\Gamma = \sum_{j=1}^{N_\Gamma} \left\{ \sum_{k=1}^{M_\Gamma} \int_{\Gamma_{\xi,\eta}} N_j(\xi, \eta) \frac{\partial G(\boldsymbol{x}(\xi, \eta), \boldsymbol{x}_l)}{\partial n} \mid \mathbf{J}^k(\xi, \eta) \mid d\xi d\eta \right\}$$

$$\phi(\boldsymbol{x}_j) = \sum_{j=1}^{N_\Gamma} \left\{ \sum_{k=1}^{M_\Gamma} E_{lj}^k \right\} \phi_j = \sum_{j=1}^{N_\Gamma} K_{lj}^n \phi_j \qquad (3.13)$$

in which, $l = 1, \ldots, N_\Gamma$, for nodes on the boundary, and $\mathbf{D}^k$ and $\mathbf{K}^d$ denote so-called local (i.e., for element k) and global (i.e., assembled for the entire discretization) Dirichlet matrices, and $\mathbf{E}^k$ and $\mathbf{K}^n$, Neumann matrices, respectively. Note, here j follows the global node numbering convention on the boundary and refers to nodal values of element k. Expressions for the Green's and shape functions, to be used in these equations are given by Eqs. (2.3) and Eqs. (3.6), respectively.

With Eqs. (3.12) and (3.13), the discretized form of the BIE (2.2) (and the equivalent BIE for $(\frac{\partial \phi}{\partial t}, \frac{\partial^2 \phi}{\partial t \partial n})$) finally reads,

$$\alpha_l u_l = \sum_{j=1}^{N_\Gamma} \{ K_{lj}^d q_j - K_{lj}^n u_j \} \qquad (3.14)$$

in which, $l = 1, \ldots, N_\Gamma$.

Boundary conditions are directly specified in Eq. (3.14); these are: (i) Dirichlet conditions for $u = \phi$ or $\frac{\partial \phi}{\partial t}$; and (ii) Neumann conditions for

$q = \frac{\partial \phi}{\partial n}$ or $\frac{\partial^2 \phi}{\partial t \partial n}$. The final algebraic system is assembled by moving nodal unknowns to the left hand side and keeping specified terms in the right hand side,

$$\{ C_{pl} + K_{pl}^n \} u_p - K_{gl}^d q_g = K_{pl}^d \overline{q_p} - \{ C_{gl} + K_{gl}^n \} \overline{u_g} \qquad (3.15)$$

where $l = 1, \ldots, N_\Gamma$; $g = 1, \ldots, N_g$, refers to nodes with a Dirichlet condition on boundary Γ_f and $p = 1, \ldots, N_p$, refers to nodes with a Neumann condition on other parts of the boundary; $\mathbf{C}$ is a diagonal matrix made of coefficients α_l.

3.1.1. *Rigid mode method*

Diagonal terms of the system matrix in Eq. (3.15) $\{C_{ll} + K_{ll}^n\}$ include both C_{ll} coefficients that can be obtained through a direct, purely geometric, calculation of solid angles θ_l at nodes of the discretized boundary, and Neumann matrix diagonal terms K_{ll}^n. As can be seen in Eq. (3.13), the latter terms contain integrals, which although regularized by the separate evaluation of their strongly singular part[61] in the form of coefficients C_{ll}, still contain a highly varying kernel that should be integrated with great care and accuracy.

Rather than directly computing these coefficients one can derive them by applying a straightforward and overall more accurate method referred to as "rigid mode"[61] by analogy with structural analysis problems. By considering a homogeneous Dirichlet problem, where a uniform field, $\overline{u} = cst \neq 0$, is specified over the entire boundary Γ (hence, $N_\Gamma = N_g$), potential flow theory implies that normal gradients q must vanish at each node. Thus, for these particular boundary conditions, Eq. (3.15) simplifies to,

$$\{ C_{jl} + K_{jl}^n \} \overline{u_j} = 0 \qquad (3.16)$$

which requires that the summation in curly brackets vanish for all l. Thus, by isolating the diagonal terms in the left-hand-side, we get,

$$\{ C_{ll} + K_{ll}^n \} = - \sum_{j(\neq l)=1}^{N_\Gamma} K_{jl}^n \qquad l = 1, \ldots, N_\Gamma \qquad (3.17)$$

which yields the value of the diagonal term of each row of Eq. (3.16) as minus the sum of its off-diagonal coefficients. These diagonal terms are directly substituted in the discretized system Eq. (3.15).

This method was earlier shown[20] to significantly improve the conditioning of algebraic systems such as Eq. (3.15), and thus the accuracy of their

numerical solution (particularly for iterative methods such as GMRES; see below).

3.1.2. *Multiple nodes*

Boundary conditions and normal directions are in general different on intersecting parts of the boundary, such as between the free surface or the bottom, and the lateral boundary of the computational domain (Fig. 1). Such intersections are referred to as 'edges', and corresponding discretization nodes as 'corners'. To be able to specify such differences, corners are represented by double-nodes, for which coordinates are identical but normal vectors are different. This double or multiple node method is essentially an extension of earlier 2D treatments.[20,59] Thus, different discretized BIE's (Eq. (3.15)) are expressed for each node of a corner multiple-node.

For Dirichlet-Neumann boundary conditions we have, for instance, equations: (i) for $l = p$, on a wavemaker boundary Γ_{r1}; and (ii) for $l = f$, on the free surface Γ_f. Since the potential must be unique at a given location, one of these two BIE's is modified in the final discretized system, to explicitly satisfy, $\phi_p = \overline{\phi_f}$ (i.e., "continuity of the potential"), where the overline indicates that the potential is specified on the free surface. For Neumann-Neumann boundary conditions at corners we have, for instance, equations: (i) for $l = p$, on a wavemaker boundary Γ_{r1}; and (ii) for $l = b$, on the bottom Γ_b. The potential continuity equation for this case reads, $\phi_p - \phi_b = 0$, both of these being unknown. Similar continuity relationships are expressed for $\frac{\partial \phi}{\partial t}$ at corners, in the corresponding BIE.

Note, at the intersection between three boundaries, triple-nodes are specified for which three BIE equations are expressed, two of which are replaced in the final algebraic system by equations specifying continuity of the potential (and of $\frac{\partial \phi}{\partial t}$).

The use of this multiple node technique makes this model especially suitable for problems involving surface piercing bodies such as wavemakers, slopes, or ships.

3.1.3. *Numerical integrations*

The discretized boundary integrals D_{lj}^k and E_{lj}^k in Eqs. (3.12) and (3.13) are evaluated for each collocation node $\boldsymbol{x}_l$ by numerical integration. When the collocation node l does not belong to the integrated element k, a standard Gauss–Legendre quadrature is applied. When l belongs to element k, the distance r in the Green's function G and in its normal gradient vanishes

at one of the nodes of the element. For such singular situations, a method of singularity extraction is used based on polar coordinate transformations. This method was first developed for a 3D-BEM using higher-order elements[58] and later applied and extended to higher-order Green's function.[62] Grilli et al.[36] optimized this method for the bi-cubic MII elements used in this model; the reader is referred to the latter reference for details.

Due to the form of Green's function Eq. (2.3), non-singular integrals may still have a highly varying kernel when the distance r becomes small, albeit non-zero, in the neighborhood of a collocation point x_l. Such situations may occur near intersections of boundary parts (e.g., such as between the free surface and lateral boundaries) or in other regions of the free surface, such as overturning breaker jets, where nodes are close to elements on different parts of the boundary. In such cases, a standard Gauss quadrature, with a fixed number of integration points, may fail to accurately calculate such integrals. One can refer to such cases as "almost" or "quasi-singular" integrals. Grilli et al.,[60] for instance, showed for 2D problems, that the loss of accuracy of Gauss integrations (with ten integration points) for such quasi-singular integrals may be several orders of magnitudes, when the distance to the collocation node becomes very small. For such 2D cases, Grilli and Svendsen[59] developed an adaptive integration scheme based on a binary subdivision of the reference element and obtained almost arbitrary accuracy for the quasi-singular integrals, when increasing the number of subdivisions. This method, however, can be computationally expensive and Grilli and Subramanya[22] developed a more efficient method that essentially redistributes integration points around the location of the quasi-singularity (point of minimum distance from an element k to the nearest collocation node, x_l). A method similar to Grilli and Svendsen's, but applicable to 3D problems, was implemented in the model[36] and showed to be both accurate and efficient in applications; the reader is referred to the latter reference for details.

3.1.4. *Solution of the algebraic system of equations*

The linear algebraic system Eq. (3.15) is in general dense and non-symmetric. Since the total number of nodes N_Γ can be very large in 3D applications, the solution by a direct method, of order N_Γ^3, as was done in 2D applications,[20,22] and in initial 3D applications of the model,[36] becomes prohibitive. Hence, for large 3D applications, an iterative solver[35] was implemented[36,53] to solve the linear system in the model, based on

a generalized minimal residual (GMRES) algorithm with preconditioning (typically the "Symmetric Successive Overrelaxation" (SSOR) method with relaxation parameter equal to 0.6), and initial solution equal to that of the earlier time step. GMRES yields a more favorable N_Γ^2 numerical complexity, similar to that of the assembling of the system matrix and is amenable to vectorization on a supercomputer. The downside with an iterative method, however, is that for the second-order time stepping scheme used here, two full systems of equations must be solved at each time step (one for ϕ and one for $\frac{\partial \phi}{\partial t}$) whereas with a direct method, the solution of the second system takes only a few percent of the time needed to solve the first system. Nevertheless, results on a CRAY-C90 showed that, for more than 2,000 nodes and a similar accuracy, the GMRES-SSOR method became faster when used in the model than the direct solution.

To tackle very large problems with a reasonable computational time, we more recently implemented the Fast Multipole Algorithm (FMA) in the model, which reduced this complexity to $O(N_\Gamma \log N_\Gamma)$. First developed by Greengard and Rokhlin[63] for the N-body problem, the FMA allows for a faster computation of all pairwise interactions in a system of N particles, and in particular, interactions governed by Laplace's equation. Hence, it is well suited to our problem. The basis of the algorithm is that due to the 3D Green's function, the interaction strength decreases with distance, so that points that are far away on the boundary can be grouped together to contribute to one distant collocation point. A hierarchical subdivision of space automatically verifies distance criteria and distinguishes near interactions from far ones. The FMA can be directly used to solve Laplace's equation, but it can also be combined with a BIE representation of this equation, whose discretization then leads to a linear system, as detailed above. Matrix-vector products in the system can be evaluated as part of an iterative solver (such as GMRES), that can be accelerated using the FMA. Rokhlin[64] applied this idea to the equations of potential theory. A review of the application of this algorithm to BIE methods can be found in Nishimura.[65] Korsmeyer et al.[66] combined the FMA with a BEM, through a Krylov-subspace iterative algorithm, for water wave computations. Following Rokhlin's ideas, they designed a modified multipole algorithm for the equations of potential theory. First developed for electrostatic analysis, their code was generalized to become a fast Laplace solver, which subsequently has been used for potential fluid flows. Their model was efficient but its global accuracy was limited by the use of low order boundary elements. Scorpio and Beck[67] studied wave forces on

bodies with a multipole-accelerated desingularized method, and thus did not use boundary elements to discretize the problem. Neither did Graziani and Landrini,[68] who used the Euler-McLaurin quadrature formula in their 2D model. Srisupattarawanit et al.[69] also used a fast multipole solver to study waves coupled with elastic structures. We show briefly below how the FMA can be combined with our model to yield a more efficient numerical tool. Details and validation of this implementation of the FMA can be found in Refs. 70 and 49. Other applications of the FMA to our model can be found in Refs. 40, 42, 43, and 46.

The FMA is based on the principle that the Green's function can be expanded in a series of separated variables, for which only a few terms need to be retained when the source point $\boldsymbol{x}_l$ and the evaluation point $\boldsymbol{x}$ are far enough from one another. Thus, for a point $\boldsymbol{O}$ (origin of the expansion) close to $\boldsymbol{x}$ but far from $\boldsymbol{x}_l$, we have,

$$G(\boldsymbol{x}, \boldsymbol{x}_l) \approx \frac{1}{4\pi} \sum_{k=0}^{p} \sum_{m=-k}^{k} \rho^k Y_k^{-m}(\alpha, \beta) \frac{Y_k^m(\theta, \varphi)}{r^{k+1}} \qquad (3.18)$$

where $\boldsymbol{x} - \boldsymbol{O} = (\rho, \alpha, \beta)$ and $\boldsymbol{x}_l - \boldsymbol{O} = (r, \theta, \varphi)$ in spherical coordinates. The functions $Y_k^{\pm m}$ are the spherical harmonics defined from Legendre polynomials. A hierarchical subdivision of the domain, with regular partitioning automatically verifying distance criteria, is defined to determine for which nodes this approximation applies. Thus, close interactions are evaluated by direct computation of the full Green's functions, whereas far interactions are approximated by successive local operations based on the subdivision into cells and the expansion of the Green's function into spherical harmonics. The underlying theory for this approximation is well established in the case of Laplace's equation. In particular, error and complexity analyses are given in the monograph by Greengard.[71]

In our case, Laplace's equation has been transformed into a BIE and a specific discretization has been used. Thus, the FMA must be adapted in order to be part of the surface wave model, but the series expansion (3.18) remains the same. Hence, with the FMA, Eq. (2.2) can be rewritten as

$$\alpha(\boldsymbol{x}_l)\, \phi(\boldsymbol{x}_l) \approx \frac{1}{4\pi} \sum_{k=0}^{p} \sum_{m=-k}^{k} M_k^m(\boldsymbol{O}) \frac{Y_k^m(\theta, \varphi)}{r^{k+1}} \qquad (3.19)$$

where moments $M_k^m(\boldsymbol{O})$ are defined as

$$M_k^m(\boldsymbol{O}) = \int_\Gamma \left\{ \frac{\partial \phi}{\partial n}(\boldsymbol{x})\, \rho^k Y_k^{-m}(\alpha, \beta) - \phi(\boldsymbol{x})\, \frac{\partial}{\partial n}\left(\rho^k Y_k^{-m}(\alpha, \beta)\right) \right\} \mathrm{d}\Gamma\,.$$

$$(3.20)$$

Instead of considering mutual interactions between two points on the boundary, we now need to look at the contribution of an element of the discretization to a collocation point. The local computation of several elements, grouped together into a multipole, relies on a BEM analysis using the spherical harmonic functions instead of the Green's function. The integration of the normal derivative of the spherical harmonics is done by taking care of avoiding an apparent singularity, which could generate numerical errors. The BEM discretization only applies to the computation of the moments. Thus, the rest of the FMA is unchanged, especially regarding translation and conversion formulas, which allow to pass information through the hierarchical spatial subdivision, from the multipole contributions to the matrix evaluation for each collocation node. In the model, the implementation of the FMA thus only affected programs that involved the assembling and the solution of the algebraic system matrix. The storage of coefficients that are used several times for each time step, for instance, is now done inside the cells of the hierarchical subdivision. The rigid mode and multiple nodes techniques, which *a priori* modified the matrix before the computation of matrix-vector products, are now considered as terms correcting the result of such products, so that the linear system keeps the same properties.

The accelerated model benefits from the faster Laplace's equation solver at each time step. The FMA model performance was tested by comparing new results with results of the former model using GMRES, for a 3D application which requires great accuracy: the propagation of a solitary wave on a sloping bottom with a transverse modulation, leading to a plunging jet.[36] The consistency of the new solution was checked but, more importantly, the accuracy and stability of results and their convergence as a function of discretization size was verified. In fact, by adjusting the parameters of the FMA, i.e. the hierarchical spatial subdivision and the number of terms p in the multipole expansions, one can essentially obtain the same results as with the former model. In this validation application, for discretizations having more than 4,000 nodes, the computational time was observed to increase nearly linearly with the number of nodes.[49,70] Using this model for other applications,[40,43,46] similar properties of the solution were observed

as a function of the discretization when applying the model to the generation of tsunamis by underwater landslides, of freak waves by directional focusing, and of waves by a moving surface disturbance, respectively.

3.1.5. *Image method*

Some applications may have a horizontal symmetry and/or a flat bottom in the computational domain. In such cases, an image method can be applied when computing the BIEs, with respect to the planes $z = -d$ and/or $y = 0$, to remove parts of the discretization. Doing so, the 3D free space Green's function is modified in the BIE, by adding contributions of each image source. Grilli and Brandini[38] show details and results of this approach in the case of the generation of extreme waves by a directional wavemaker over a flat bottom. The image method was also applied for a horizontal symmetry to compute cases of wave generation by underwater landslides,[42,43] and for a flat bottom and a horizontal symmetry, to the generation of waves by a moving disturbance on the free surface, over a flat bottom.[54]

Note, in the FMA, when the original source point is far from the collocation point, so are the images. Thus, image contributions are simply added to the multipole associated with the original point. In the usual application of the FMA, images should be accounted for at a coarser subdivision level than that of the original source points, since they are further away from the evaluation point.

3.2. *Time integration*

A second-order explicit scheme based on Taylor series expansions is used to update the position $\boldsymbol{R}$ and velocity potential ϕ on the free surface, as,

$$\boldsymbol{R}(t + \Delta t) = \boldsymbol{R} + \Delta t \frac{\mathrm{D}\boldsymbol{R}}{\mathrm{D}t} + \frac{\Delta t^2}{2} \frac{\mathrm{D}^2 \boldsymbol{R}}{\mathrm{D}t^2} + O\left(\Delta t^3\right) \qquad (3.21)$$

$$\phi(t + \Delta t) = \phi + \Delta t \frac{\mathrm{D}\phi}{\mathrm{D}t} + \frac{\Delta t^2}{2} \frac{\mathrm{D}^2 \phi}{\mathrm{D}t^2} + O\left(\Delta t^3\right) \qquad (3.22)$$

where Δt is the varying time step and all terms in the right-hand sides are evaluated at time t.

First-order coefficients in these Taylor series are given by Eqs. (2.4) and (2.5), which requires calculating ϕ, $\partial \phi / \partial n$ at time t on the free surface. Second-order coefficients are obtained from the Lagrangian time derivative

of Eqs. (2.4) and (2.5), as

$$\frac{\mathrm{D}^2 \boldsymbol{R}}{\mathrm{D}t^2} = \frac{\mathrm{D}\boldsymbol{u}}{\mathrm{D}t}$$
$$\frac{\mathrm{D}^2 \phi}{\mathrm{D}t^2} = -gw + \boldsymbol{u} \cdot \frac{\mathrm{D}\boldsymbol{u}}{\mathrm{D}t} - \frac{1}{\rho}\frac{\mathrm{D}p_a}{\mathrm{D}t} \,. \tag{3.23}$$

Appendix A.1 gives the expression for the Lagrangian acceleration on the boundary, which requires calculating $(\frac{\partial\phi}{\partial t}, \frac{\partial^2\phi}{\partial t\partial n})$ at time t, as well as their tangential derivatives. As mentioned above, this is done by solving a second BIE similar to Eq. (2.2) for $\frac{\partial\phi}{\partial t}$. Since both BIEs correspond to the same boundary geometry, the resulting linear algebraic system Eq. (3.15) only needs to be discretized and assembled once. Boundary conditions for the second BIE are expressed based on the solution of the first BIE. On the free surface, Bernoulli equation yields the Dirichlet condition,

$$\overline{\frac{\partial\phi}{\partial t}} = -gz - \tfrac{1}{2}\,\boldsymbol{\nabla}\phi\cdot\boldsymbol{\nabla}\phi - \frac{p_a}{\rho} \qquad \text{on } \Gamma_f(t)\,. \tag{3.24}$$

For wave generation by a moving boundary, such as a wavemaker (active or absorbing) or an underwater landslide, of velocity $\boldsymbol{u}_p(\boldsymbol{x}_p, t)$ and acceleration $\dot{\boldsymbol{u}}_p(\boldsymbol{x}_p, t)$, using Eqs. (2.6) and (2.24), and after some derivations, we obtain the Neumann condition,

$$\overline{\frac{\partial^2\phi}{\partial t\partial n}} = \dot{\boldsymbol{u}}_p \cdot \boldsymbol{n} + \boldsymbol{u}_p \cdot \dot{\boldsymbol{n}} - \phi_n\phi_{nn} - \frac{1}{(1-\kappa^2)^2}\bigg\{(\phi_s - \kappa\phi_m)$$
$$(\phi_{ns} - \kappa\phi_{nm}) + (\phi_m - \kappa\phi_s)(\phi_{nm} - \kappa\phi_{ns})\bigg\} \tag{3.25}$$

where the expression for ϕ_{nn} is given in Appendix A.1 and $\dot{\boldsymbol{n}} = \boldsymbol{\Omega}\times\boldsymbol{n}$ for a rigid body motion with angular velocity $\boldsymbol{\Omega}$.

On stationary boundaries we simply specify,

$$\overline{\frac{\partial^2\phi}{\partial t\partial n}} = 0 \qquad \text{on } (\Gamma_{r2}), (\Gamma_b) \tag{3.26}$$

depending on the considered problem.

Time step Δt in Eqs. (3.21) and (3.22) is adaptively selected at each time to satisfy a mesh Courant condition,

$$\Delta t = C_0 \frac{\Delta r^{\min}}{\sqrt{gh}} \tag{3.27}$$

where C_0 denotes the Courant number, $\Delta r^{\min}$ is the instantaneous minimum distance between two neighboring nodes on Γ_f and h is a characteristic

depth. Grilli et al.[36] performed a sensitivity analysis of numerical errors in the model (see next section) to the spatial and temporal discretization expressed as a function of the mesh size and Courant number. They showed that errors were minimum for $C_0 = 0.45$ to 0.5. This is the value used in the present applications.

This second-order time stepping scheme is explicit and uses all spatial derivatives of the field variables at time t to calculate the position and potential of water particles at $t + \Delta t$. This was shown in earlier applications to provide a good stability of the computed solution, which typically can proceed for thousands of time steps without requiring any smoothing.

Note that for absorbing wavemaker boundaries, the piston position is updated for the next time step using Taylor series expansions similar to those used for the free surface.

3.3. *Numerical errors*

In a number of earlier applications of the model to cases with known analytical solution, it was confirmed that maximum local numerical errors in the BEM are of more than third-order in mesh size $\Delta r^{\min}$ (typically 3.5-4th-order[46]), which is expected considering the third-order boundary elements used in the discretization. For a given mesh size, numerical errors were also shown to be of third-order in time step Δt, when mesh size was such as to satisfy the Courant condition Eq. (3.27).

For general nonlinear wave generation and propagation problems, when no a priori solution is known, the mesh size is selected based on expected wavelength in order to have a sufficient resolution of individual waves. Time step is then adaptively adjusted based on Courant condition Eq. (3.27). An estimate of numerical errors can thus only be made in a global sense. For instance, the global accuracy of the BEM solution can be checked at each time step by calculating a nondimensional error on boundary flux continuity as,

$$\varepsilon_C = \frac{\Delta t}{V_o} \int_\Gamma \frac{\partial \phi}{\partial n} \, \mathrm{d}\Gamma \tag{3.28}$$

where V_o denotes the initial domain volume.

The combined global accuracy of the BEM solution and time stepping scheme can then be estimated as a function of time, by checking the conservation of volume,

$$V(t) = \int_\Gamma z n_z \, \mathrm{d}\Gamma \tag{3.29}$$

and total energy,

$$E(t) = \tfrac{1}{2}\, \rho \int_\Gamma \left(\phi \frac{\partial \phi}{\partial n} + g z^2 n_z \right) \mathrm{d}\Gamma \qquad (3.30)$$

where the first and second terms represent the kinetic and potential energy contributions of the flow respectively, and n_z is the vertical component of the unit normal vector. Thus, a time varying nondimensional error on volume conservation can be expressed as $\varepsilon_V = (V - V_o)/V_o$ while for the energy, the nondimensional error on total energy reads, $\varepsilon_E = (E - E_o)/E_o$. However, to calculate the latter error, one must either start from an initial wavefield with total energy E_o or wait for the model to achieve a quasi-steady state, with nearly constant time average energy, expressing a balance between wave generation and dissipation/absorption. Such error calculations for complex propagating and shoaling wave fields, dissipating their energy in an AB, were made extensively for 2D computations.[23]

As mentioned above, it was found in applications that errors on volume and energy conservation reach a minimum for $C_0 \simeq 0.45$ to 0.5, independently of mesh size. This implies in particular that Δt could not be imposed too small, otherwise numerical errors would accumulate faster when solving the BIEs at intermediate times. It is emphasized that no smoothing/filtering was used to stabilize the solution in all cases we considered in past applications as well as those reported later in this paper.

3.4. *Mesh regridding and time updating*

Due to the MEL time updating of the free surface nodes (identical to water particles), during computations of wave propagation, nodes may accumulate in some areas of the free surface (e.g., with converging flow such as overturning breaker jets) or move away from some areas (such as a wavemaker boundary generating nonlinear waves with a non-zero mean mass flux).

Hence, although this is not required in most cases to stabilize computations, it is desirable to have a means in the model of both refining the mesh discretization in areas of formation of breaker jets, prior to their occurrence or to periodically regrid sections of the free surface on a regular mesh. In 2D studies, regridding was done by implementing a node regridding method in which a specified number of nodes were regridded at constant arclength value in between two nodes selected on the free surface.[22] In the initial implementation of the 3D model,[36] a two-dimensional regridding method was implemented based on this principle. For practical reasons, the 3D

regridding method required the free surface $\eta(x, y)$ to be single-valued. In other more recent applications, a pseudo-Lagrangian time updating was implemented,[45,46] in which free surface nodes can move at a velocity different from the flow velocity. By adjusting this velocity, free surface nodes can be updated on a purely Eulerian manner (i.e., vertically) in some regions of the boundary or on a fully Lagrangian matter in other regions, and all the range in between. The reader is referred to the published references for more information on this matter.

4. Numerical Results

4.1. *Shoaling and breaking of solitary waves on a sloping ridge*

After implementing the model, Grilli et al.[36] first tested its accuracy and efficiency by computing the propagation of the simplest possible nonlinear wave with numerically exact shape and potential, i.e., a solitary wave. Tanaka[51] developed a method for calculating fully nonlinear solitary wave shape and kinematics up to their maximum height of about 80% of the local constant depth. Grilli and Svendsen[59] adapted this method to calculating initial solitary solutions in their 2D model, and Grilli et al.[5,6] then calculated physical features for the shoaling and overturning of such waves over a variety of slopes. Upon implementing the 3D model,[36] such exact solitary waves propagating over constant depth and plane slopes were also used to validate the model and estimate the required spatial and temporal discretization sizes; this led to the optimal value of the mesh Courant number discussed before. To produce well-controlled 3D overturning jets, they then calculated the shoaling of solitary waves over a sloping ridge causing 3D focusing. Fochesato et al.[50] later used similar test cases to validate their implementation of a modified surface representation in the model. Since shallow water wave breaking on sloping beaches exhibits many of the features of a succession of solitary waves, Guyenne and Grilli[53] performed a detailed numerical study of the physics of 3D overturning waves over arbitrary bottom, using the same idealized case of a solitary wave shoaling over a sloping ridge. They analyzed shoaling and breaking wave profiles and kinematics (both on the free surface and within the flow) and observed that the transverse modulation of the ridge topography induces significant 3D effects on the time evolution, shape and kinematics of breaking waves. These effects were found to be similar to those observed for periodic 3D
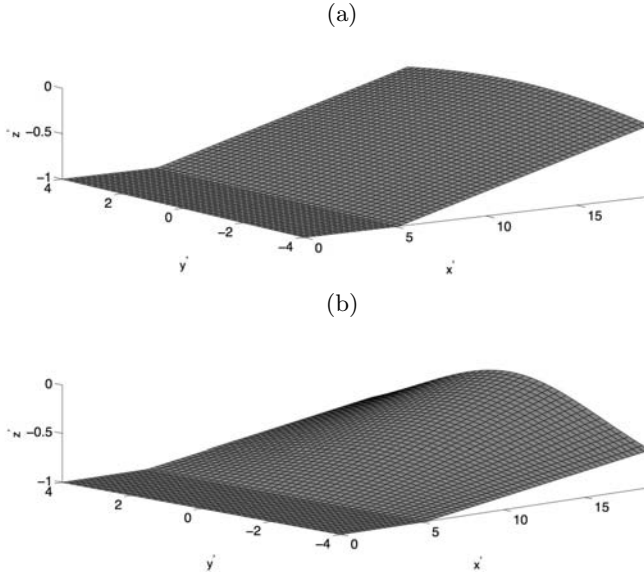
(a)

(b)

Fig. 4.   Bottom topography and its initial discretization for the shoaling of a solitary wave over a sloping ridge with a $1:15$ slope in the x-direction and a lateral $\operatorname{sech}^2(ky')$ modulation. Configurations with $k =$ (a) 0.1; and (b) 0.25 are represented here.

overturning waves in deep water.[35] Comparing earlier 2D results[3,19] to 3D results in the middle cross-section of the ridge, Grilli and Guyenne showed remarkable similarities, especially for the shape and dynamics of the plunging jet, indicating that late in the overturning, wave breaking is quasi-2D and becomes almost independent from the background flow and boundary conditions (including bottom topography), that have induced breaking.

Solitary wave breaking on a sloping ridge is illustrated in the following. Figure 4 shows the typical sloping ridge geometry used.[53] [Primes hereafter indicate non-dimensional variables based on long wave theory, i.e. lengths are divided by h_0 and times divided by $\sqrt{h_0/g}$.] The ridge starts at $x' = 5.225$, with a $1:15$ slope in the middle cross-section and a transverse modulation of the form $\operatorname{sech}^2(ky')$. Here, we successively set $k = 0.1$ and 0.25, which correspond to different amplitudes for the transverse tails of the ridge. An incident 'Tanaka' solitary wave of height $H' = 0.6$ with the crest located at $x'_0 = 5.785$ for $t' = 0$ is used in computations.

The computational domain is of width 8 or $16h_0$, for each case respectively, in the y-direction and is truncated at $x' = 19$ in the x-direction,

with minimum depth $z' = -0.082$ in the middle ($y' = 0$). The initial discretization for the bottom and free surface consists of 50×20 or 40 quadrilateral elements in the x- and y-directions, respectively ($\Delta x'_0 = 0.38$ and $\Delta y'_0 = 0.4$). The lateral boundaries have grid lines connecting the edge nodes of the bottom and free surface, with four elements specified in the vertical direction. Consequently, the total number of nodes is $N_\Gamma = 2862$ or 5102, and the initial time step is set to $\Delta t'_0 = 0.171$ for $C_0 = 0.45$. Computations are performed in this initial discretization as long as global errors on wave mass remain acceptable (i.e., less than 0.05% or so). A two-dimensional regridding to a finer resolution is then applied at a time when the wave profile is still single-valued. The discretization is increased to 60×40 or 70 quadrilateral elements, respectively, in the portion $8 \leq x' \leq 19$ of the bottom and free surface ($\Delta x' = 0.18$, $\Delta y' = 0.2$ and $N_\Gamma = 6,022$ or 9,982). For instance, regridding was applied at $t' = 4.900$ for $k = 0.25$, when errors on volume and energy conservation are 0.010% and 0.013% respectively.

Figure 5 shows results just before jet touch-down, at a time when global errors on mass and energy are still acceptable (typically less than 0.1% with respect to initial wave mass or energy). Figure 5a shows wave shapes for $k = 0.1$ at $t' = 8.958$, seen from two different angles, and Fig. 5b shows results for $k = 0.25$ at $t' = 9.268$. In the former case, the wave develops into a wide barely modulated breaker while in the latter case, for which the incident wave propagates over a laterally steeper ridge, the overturning wave develops into a narrow, well developed and more strongly plunging jet. These computations were performed in 2003-04, using GMRES as a solver, on a single processor Compaq Alpha GS160 computer. Without any particular optimization, the CPU time per time step for $N_\Gamma = 6,022$ was of $O(10)$ minutes (for a few hundred time steps). As we shall see, a much faster solution was achieved for more recent computations using the FMA method in combination with GMRES.

The model is general and various cases of breaking induced by complex nearshore bathymetry can be simulated. Figure 6, for instance, shows the breaking of a solitary wave over a sloping bar, a case that would be of interest for studying the sensitivity of wave-induced nearshore currents to breaker characteristics and bar shape, designing submerged breakwaters used for coastal protection, or surfing reefs aimed at inducing certain breaker types and shape. For more results, details, and discussion of the physics of 3D overturning waves over shallow water topography, the interested reader is referred to the literature.[53]
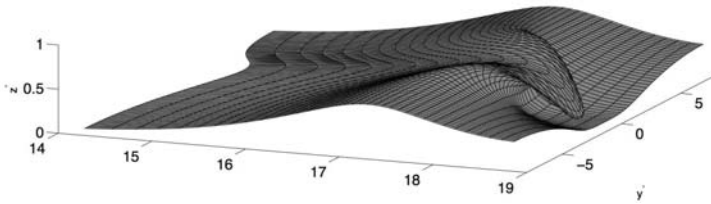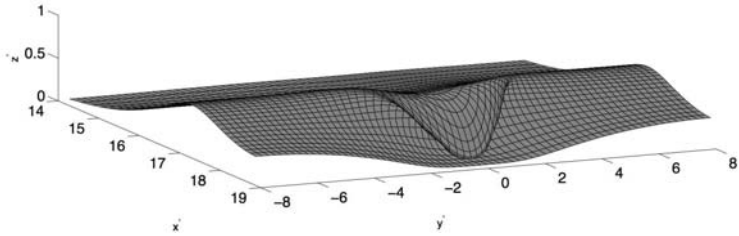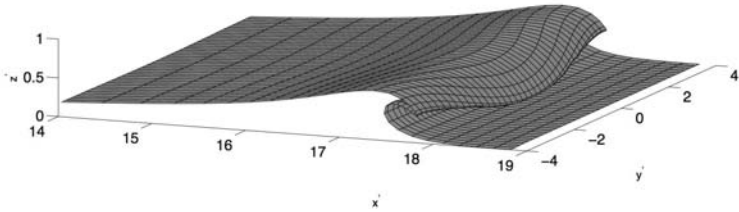
(a)
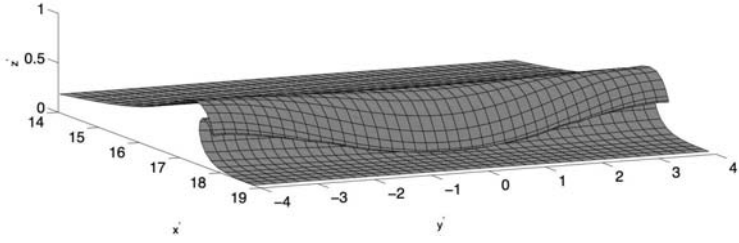
(b)

Fig. 5.   Solitary wave profiles for (a) $k = 0.1$ ($t' = 8.958$), (b) $k = 0.25$ ($t' = 9.268$).
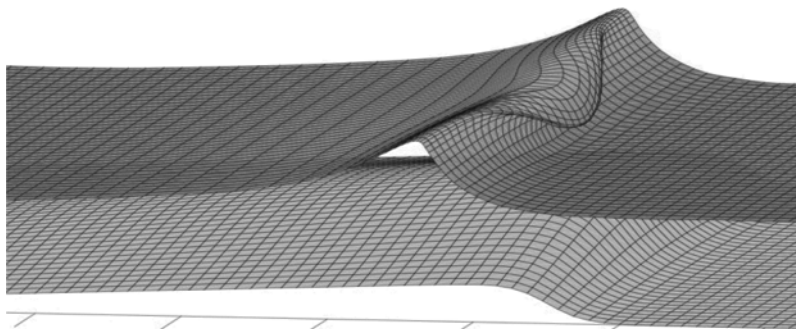
Fig. 6.   Example of solitary wave breaking over a sloping bar.

4.2. *Generation of extreme waves by directional energy focusing*

Three-dimensional directional wave energy focusing is one of the mechanisms that contribute to the generation of extreme gravity waves in the ocean, also known as rogue waves. Grilli and Brandini[38,39] and Fochesato et al.[40] used the 3D-BEM FNPF model to simulate and analyze this phenomenon over constant depth, by specifying the motion of a snake wavemaker on one side of the model boundary and an open snake absorbing boundary on the other side, thus creating a 3D Numerical Wave Tank (NWT). The wavemaker law of motion was specified such as to linearly focus periodic waves in the middle of the tank.[72] Using the image method in the z direction to reduce the size of the discretization initial stages of 3D extreme breaking waves were simulated.[38,39] Computations however could not proceed further, in part because of the lack of resolution of the breaker jet and because the more accurate free surface representation developed later[50] was not used. By contrast, in more recent work,[40] all model improvements detailed in this paper were used, including the image method in both y and z directions, and the FMA combined with GMRES as a solver, whose efficiency made it possible to generate finely resolved 3D focused overturning waves and analyze their geometry and kinematics. In the following, we only present a typical simulation of an overturning rogue wave. A literature review, and further computations and sensitivity analyses of extreme wave geometry and kinematics to water depth and maximum angle of directional energy focusing can be found in Ref. 40. In particular, in the latter work, we show that an overturning rogue wave can have

different properties depending on whether it is in the focusing or defocusing phase at breaking onset. The maximum focusing angle and the water depth largely control this situation, and therefore the main features of the rogue wave crest, such as its 3D shape and kinematics.

In the following application, we generate an overturning rogue wave by specifying the superposition of 30 wave components at the snake wave-maker. These wave components have identical frequency $\Omega = 0.8971$ rad/s (i.e., linear period of $T = 7$ s, linear wavelength $L = 2\pi/k = 72$ m, in depth $d = 20$ m) and amplitude $A = 0.19$ m, but directions varying between -45 and 45 degrees. With these parameters, linear wavemaker theory yields a stroke amplitude of $a = 0.2$ m for each individual wave. The amplitude at the linear focal point (specified here at the distance $x_f = 250$ m from the wavemaker) would thus theoretically be $A^* = 6.3$ m. This is clearly a large value, in accordance with our goal of generating a large overturning wave early in the generation process, before the wave reaches the far end of the tank where, despite the absorbing boundary condition, some reflection may occur that may perturb wave focusing. The NWT used in this computation has a 440 m length (or $22d$) and a 600 m width (or $30d$). For the selected focusing distance, this NWT length is such that, when overturning of the extreme wave occurs, only very few small waves will have reached the far end of the tank. Hence, the absorbing boundary condition will barely be activated in this computation. The half width of the NWT along y is divided into 70 elements ($\Delta y = 4.3$ m), and its depth into 4 elements. At the beginning of computations, the discretization has 90 elements in the $x-$longitudinal direction ($\Delta x = 4.9$ m), which corresponds to roughly 15 nodes per wavelength, which makes a total of $N_\Gamma = 7,626$ nodes (considering the image method eliminates the bottom and one lateral boundary). In order to better resolve the wave steepening towards breaking (defined as the occurrence of the first vertical tangent on the free surface), the x-resolution is later improved by using 120 elements with an irregular grid, refined around the breaking wave for $t > 43.39$ s ($= 6.20T$), bringing the total number of nodes to $N_\Gamma = 9,906$. The present simulations using the FMA required 2 min per time step (in scalar mode) on a biprocessor Xeon (3Ghz, 2Gb of RAM) and lasted for more than 350 time steps (i.e., a total of 700 min). Although processors clearly differ, such computational times per time step are clearly much faster than in the previous application that only used GMRES as a solver.

Figure 7 shows the free surface elevation at a time the focused wave has started to overturn. A detailed analysis of the earlier stages of this
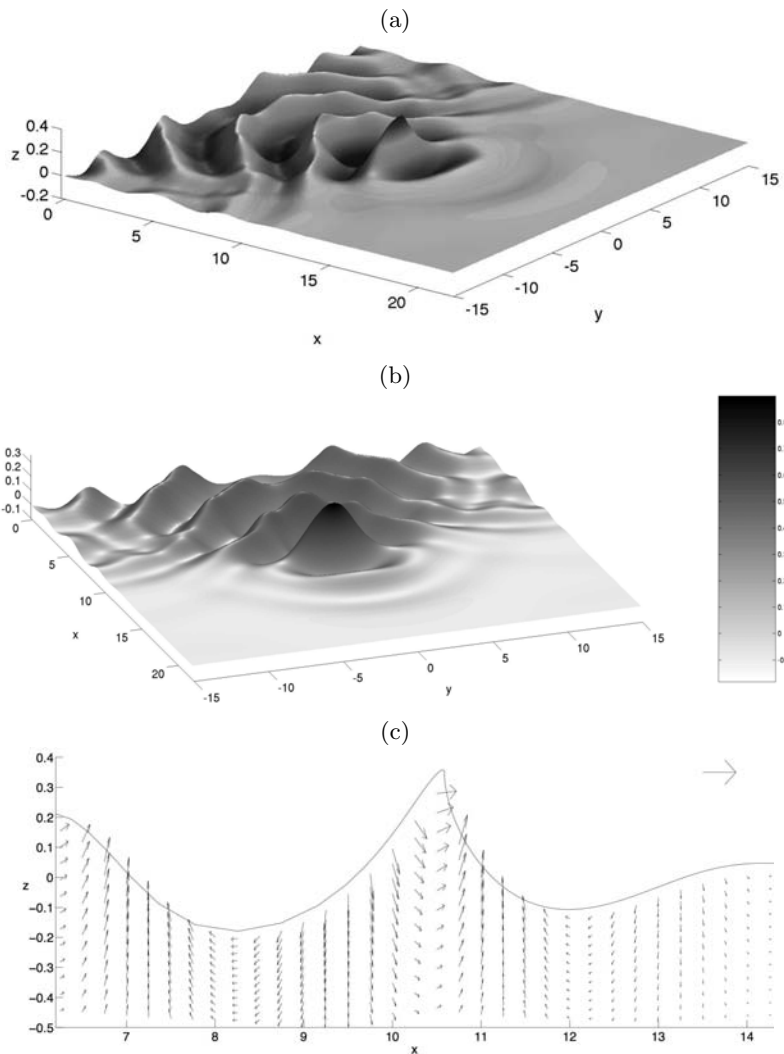
(a)

(b)

(c)

Fig. 7.　Free surface evolution of focused wave shown at $t = 6.89T$, when overturning starts, with the wave crest located at $x = 211$ m (or 10.55 d): (a) wave elevation in arbitrary gray scale; (b) wave horizontal velocity $u/\sqrt{gd}$; (c) vertical section at $y = 0$, with the arrows showing the projected internal velocity vectors (the arrow in the upper-right corner represents the unit nondimensional velocity vector; the vertical axis scale is exaggerated by a factor of 9). [Note that contours shown in this figure are less smooth than the actual wave surface in the BEM, because of the plotting algorithm.]

computation would show that the initially flat NWT free surface starts oscillating near the wavemaker and, due to the ramp-up of the wavemaker motion specified over three wave periods, a first moderate amplitude wave is generated. This first wave then almost disappears at the plot scale while the wavemaker amplitude of oscillations further increases, to give rise in the middle of the tank to an even larger wave and, eventually, after the ramp-up is over to achieve complete focusing, with an even larger wave, that starts overturning around $x_c = 211$ m (or 10.55 d) as shown in Fig. 7a. This is closer to the wavemaker than the linearly estimated focal point (12.5d). Behind this breaker, we see on the figure that the phenomenon is starting to repeat itself, with a new curved crest line appearing and converging towards the center of the NWT. Figure 7b shows the horizontal velocity component $u/\sqrt{gd}$ values over the free surface; we see that, at overturning, very large values only occur in the upper third of the focused wave crest, approaching 0.9 at the wave crest tip, while the wave linear phase speed is $c/\sqrt{gd} = 0.73$. The focused wave crest thus tends to move forward faster than the phase velocity of its basic wave components, thus initiating overturning and breaking. The cross-section in Fig. 7c shows internal velocity fields, which illustrate the more intense kinematics at incipient breaking immediately below the wave crest. The full 3D fields would show that particle velocities are essentially upwards, with the upper part of the fields having nearly uniform values. Accelerations are negative, with greater values ($\simeq 2g$) nearest the crest.

The properties of this extreme focused wave agree qualitatively well with observed characteristics of rogue waves. Figure 7a shows a circular trough located just in front of the overturning wave (the so-called "hole in the sea" reported by rogue wave eyewitnesses). Behind the wave, an even deeper trough has formed (which is more clearly seen in Fig. 7c), separating the main wave from the curved crest line that follows it. This trough has more of a crescent shape, due to the directions of the incoming waves. Due to the significant directionality, the overturning part of the wave is quite narrow and also located in the middle of a curved front, hence illustrating strong 3D effects. The amplitude of the overturning wave is significantly larger than that of the following waves, which have not yet converged, and the wave has a strong back-to-front asymmetry (this is also more clearly seen in Figs. 7c and 8). In the vertical cross-section of Fig. 7c the wave profile appears similar to that observed in rogue wave measurements or observations (see for example the extreme wave measured under the Draupner platform in the North Sea on January 1st 1995), as well as in earlier 2D numerical
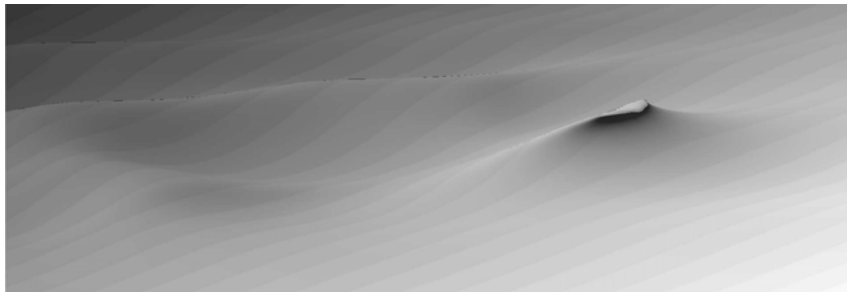
Fig. 8.   Close-up of the overturning rogue wave for case of Fig. 7.

studies, for instance those related to modulational instabilities of a wave packet.[73] A large crest ($A_c = 7.16$ m or $0.358d$) is preceded and followed by two shallower troughs; the back trough is deeper than the front one ($A_{t1} = 3.60$ m and $A_{t2} = 2.14$ m, or $0.180d$ and $0.107d$, respectively). Wave height is $H_1 = A_c + A_{t1} = 10.76$ m or $0.538d$, which is less than the linearly predicted upper bound value $2A^* = 12.6$ m. This is because of the early breaking of the wave and the incomplete focusing. The wavelength of the nonlinear focused wave can be estimated to $\lambda \simeq 78.0$ m (or 3.90 d), by averaging the rear and front wavelengths, which is more than the linear value, due to amplitude dispersive effects. This yields a steepness $H/\lambda = 0.138$, which is greater than the limiting steepness predicted by Miche's law for this depth (about 0.132 for a symmetric maximum Stokes wave). Hence, the asymmetric and transient 3D extreme wave generated in the NWT in this application grows further than the theoretical limiting steepness, before it overturns. This may have important implications for structural design of offshore structures (e.g., Ref. 74). Finally, Fig. 8 shows a closeup of the development of the plunging jet in Fig. 7. We did not attempt to accurately follow the overturning jet beyond this stage, although as seen in the previous application, the model is clearly capable of doing so, given a proper discretization. Hence, here, we did not discuss wave breaking characteristics in detail, but limited our analyses to the initiation of breaking. Note nevertheless the similarity of this 3D breaking crest with some of the shallow water breaking waves shown in the previous section and in Ref. 53.

More computational cases and further discussions can be found in Ref. 40.

4.3. *Landslide tsunami generation*

While the scientific community has worked for decades on the modeling of
tsunamis directly generated by the bottom motion caused by an earthquake
(so-called co-seismic tsunamis), in the past ten years, the 1998 Papua New
Guinea (PNG) tsunami has focused the interest of a sizeable part of the sci-
entific community on the lesser studied landslide tsunamis. After years of
field surveys and modeling work following the PNG event, an almost unan-
imous consensus was reached in the community that the large tsunami,
whose coastal runup on the nearby shore reached 16 m at places, while
associated with a moderately tsunamigenic 7.1 magnitude earthquake, had
been triggered by an underwater mass failure, itself triggered (with a 15
min. delay) by the earthquake (e.g., ground acceleration and induced ex-
cess groundwater pore pressure). Field work further showed that the mass
failure responsible for the triggering of the tsunami was a large rotational
slide (i.e., a slump), of at least 6 km^3, initiated at an average depth of
1,500 m, about 60 km offshore of the main impacted area of PNG (see, e.g.,
Ref. 75 for a recent review of this event, including field work and modeling).

Thus, following PNG, a number of laboratory and modeling stud-
ies were conducted, aimed at better understanding the physics of land-
slide tsunami generation and relating initial tsunami parameters (i.e., the
tsunami source), to geometrical, geological, and geotechnical parameters of
the underwater slide. In most of the work so far, the more complex trig-
gering phase was largely ignored to concentrate on tsunami generation by
the moving underwater slide. While tsunamis, once generated, eventually
behave in the far field as long gravity waves, which in deep water can even
be well approximated by linear long wave theory, near their source, land-
slide tsunamis are generated by the complex 3D flow field induced by the
moving slide. Moreover, if the slide is initiated in very shallow water (or is
partly emerged as a so-called subaerial slide), initial waves may be strongly
nonlinear or even breaking.

In view of these features of landslide tsunamis and to address the prob-
lem in the most general manner from the fluid point-of-view, Grilli and
Watts[76] developed a 2D-FNPF model of landslide tsunami generation and
initial propagation. The slide law of motion in this model was that of a
solid body moving down a plane slope, under the action of gravity, buoy-
ancy, basal friction, hydrodynamic drag and inertia (added mass) forces.
Grilli and Watts[77] performed additional work in this direction, and applied
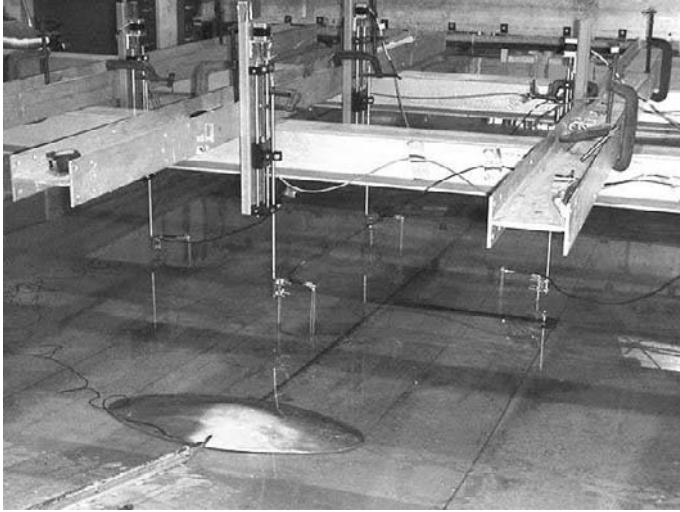an updated version of this initial model to a large set of parameters, in

Fig. 9.   General view of experimental set-up for landslide tsunami experiments: slope, rail, landslide model, wave gauges/step motors, and supporting I-beams.
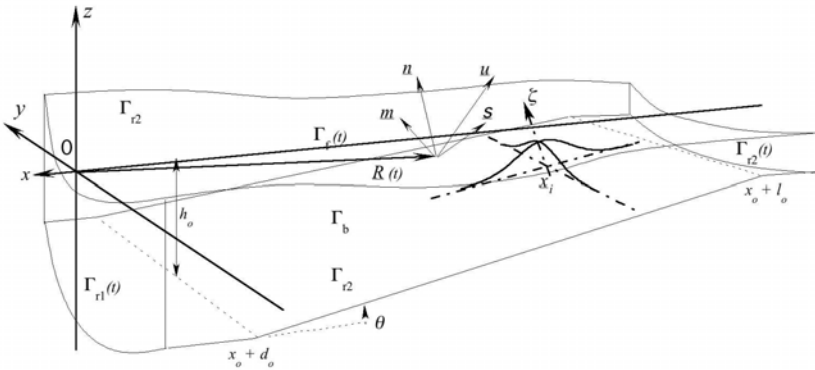

Fig. 10.   BEM domain and variable set-up for 3D-FNPF computations of landslide tsunami generation.

combination with 2D laboratory experiments used for validation. In particular, these authors showed that most of the tsunami generation occurs for $t < t_0 = u_t/a_0$, a characteristic time, function of the slide terminal velocity u_t and initial acceleration a_o, both of these being themselves functions

Fig. 11.   Example of experimental surface elevations generated for $d = 0.12$ m at $t \simeq t_o$. Note, the submerged model slide is visible underwater at the top of the picture.

of the problem parameters. Based on this numerical work, Watts et al.[78] developed semi-empirical relationships expressing the main tsunami characteristics (such as initial depression) as a function of the slide parameters (for both translational landslides and slumps). Such relationships allowed to rapidly design a 3D landslide tsunami source and conduct case studies, using more standard long wave models (see Ref. 79 for details). While it was shown that landslide tsunamis are fairly directional and, hence, 3D effects in their sources are less prominent than for co-seismic tsunami sources, Grilli et al.[41] performed 3D-FNPF landslide tsunami simulations, by modifying the present FNPF model. Enet and Grilli[42,43,80] later performed large scale 3D laboratory experiments that validated both results of this model, as well as the empirical relationships developed earlier, based on 2D simulations. They also performed new simulations of their 3D experiments, using the more recent and optimized version of the 3D-FNPF model detailed in this paper.

The following illustrates some of these 3D landslide tsunami simulations and their experimental validation; more results and details can be found in the references. Figure 9 shows the experimental set-up for the earlier experiments.[42,80]   A smooth bi-Gaussian-shaped aluminum body (length $b = 0.395$ m, width $w = 0.680$ m, and maximum thickness $T = 0.082$
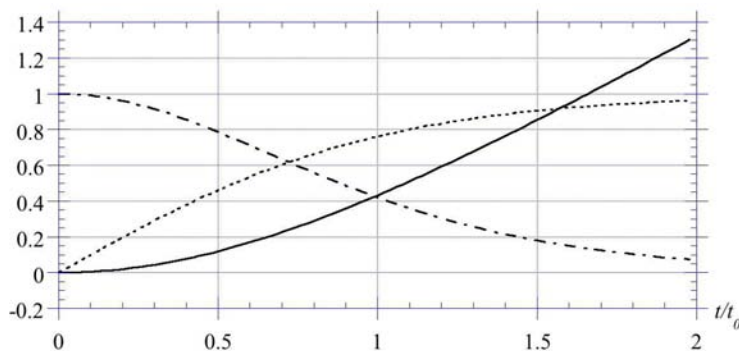
Fig. 12.   Typical laws of motion for rigid underwater landslides, as a function of non-dimensional time t/t_o: dimensionless motion parallel to the slope s/s_0 (——), velocity u/u_t (- - - -), and acceleration a/a_0 (— - —), where (s_0, u_t, a_0) denote characteristic distance of motion, terminal velocity, and initial acceleration, respectively, all function of the slide and set-up physical parameters.

m) is used to represent a solid underwater slide moving down a 15° slope, from a series of initial submergence depths d. [This shape reduces flow separation and hence makes potential flow theory fully relevant to model such cases.] Experiments were performed in the 3.6 m wide, 1.8 m deep and 30 m long wavetank of the Department of Ocean Engineering, at the University of Rhode Island. Figure 10 shows the BEM model set-up used in numerical simulations, which is similar to the earlier work,[41] but uses two absorbing pistons, open boundaries, in the negative and positive x directions, representing the onshore and offshore directions, respectively. A shallow shelf of depth h_1 is modeled onshore of the slide, while the depth levels-up to h_o offshore of the slide. As mentioned, the model uses the image method to remove half of the unknowns for $y < 0$ and the FMA (combined with GMRES) is used for the BEM solution at each time step. For these simulations, which were performed on a PC-Pentium computer circa 2005, this led to about 4 min per time step for $N_\Gamma = 4146$ nodes (half domain).

Landslide motion, and the corresponding deformation of the bottom discretization, are specified as a boundary condition, based on laws of motion derived earlier[77] and adapted to the 3D model[80] (Fig. 12). Note that the landslide is represented in the BEM model as a space and time varying "wave" of elevation z, specified for the bottom elements (of fixed coordinates x and y) located on the underwater slope, between $x = x_o + l_o$ and
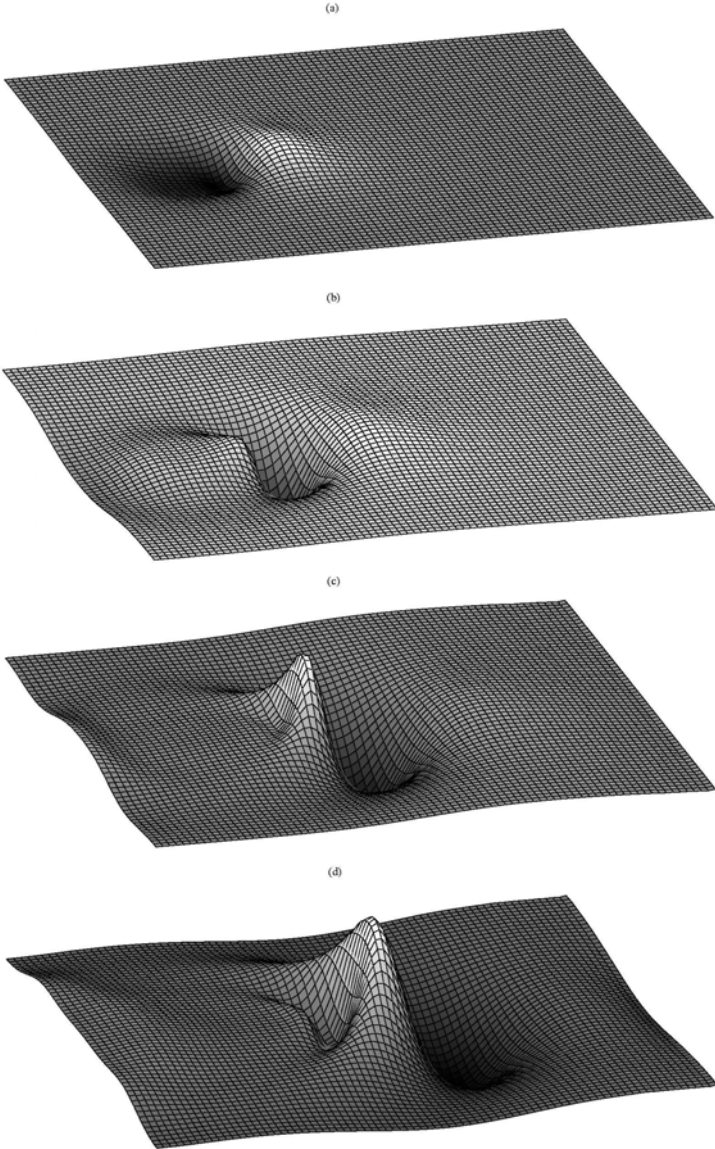
Fig. 13.   Landslide tsunami shapes computed at $t = t_0/4$; (b) $t_0/2$; (c) $3t_0/4$; and (d) t_0, for initial slide submergence $d = 120$ mm, for which $t_0 = 1.74$ s at laboratory scale (vertical scale is exaggerated).
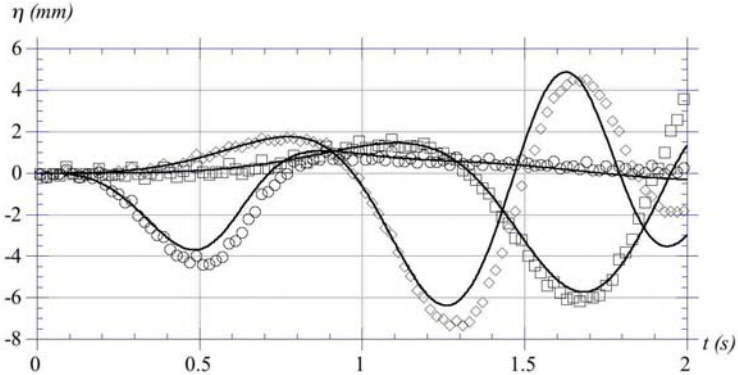
Fig. 14. Comparison of experiments (symbols) with model results (——) for $d = 0.140$ m at gauge: 1 ∘; 2 ◇; and 4 □ (only 10% of experimental data points are shown).

$x_o + d_o$ (see Fig. 10, and[41] for detail). Figure 13 shows typical free surface elevations computed at various times $t \leq t_0$ for an initial slide submergence $d = 0.12$ m. Figure 11 shows a picture of the free surface observed in the tank at the time of Fig. 13d. Both observed and simulated surfaces exhibit a typical double crescent-shaped crests, in a $\simeq 30°$ angular sector centered in the direction x of slide motion. Figure 14 shows a comparison of numerical simulations with experiments for $d = 0.14$ m (for which $t_0 = 1.87$ s), for 3 wave gauges. [Note, in these simulations, in order to more closely model tank experiments, only one absorbing boundary was used on the offshore side of the NWT, while the length of the onshore shelf, of depth h_1 was adjusted to yield the same volume as for the sloping bottom.] The agreement between both of these is quite good, with absolute differences between computations and measurements on the order of 1 mm, which considering meniscus effects on the wave gauges, is within the experimental error. The first gauge (1) is located above the initial middle location of the slide at $x_i = 0.846$ and $y = 0$ (Fig. 10), and essentially records the initial tsunami depression induced by the slide motion (4 mm at model scale; also see Fig. 13b). As expected, this surface depression, which represents the initial tsunami generation (i.e., source), occurs for $t < 0.5t_0$. At later times, the depression 'rebounds' into large offshore propagating oscillatory waves, gradually spreading with a leading depression wave, and smaller onshore propagating waves (causing coastal runup), indicating strong dispersive effects (see Fig. 13). Gauge (2) is located further downslope and off-axis, at

$x = 1.469$ m and $y = 0.35$ m. Here, the tsunami has developed into a dispersive train (see Ref. 80 for longer time series of experimental measurements) whose first wave has a 11-12 mm height. Finally, at gauge (4), further offshore and off-axis at $x = 1.929$ m and $y = 0.50$ m, the tsunami also has an initial depression followed by a train of oscillatory waves. The interested reader will find more cases and details of experiments and simulations in Refs. 42,43 and 80.

4.4. *Waves generated by a surface disturbance*

In recent years there has been broad interest in high speed ships, not only for special purpose military crafts, but also for fast passenger ferries and commercial sealift. In this respect, one of the most promising concepts is the Surface Effect Ship (SES), which features an air cushion located, unlike hovercrafts, within a cavity built in a rigid hull. Numerical simulations were conducted with the 3D-FNPF model, as part of the design of a new type of SES with catamaran hull (the Harley SES), which also involved performing tow tank experiments and analyses with a 2.3 m long SES model. Specifically, among various resistance terms, experimentally measured wavemaking drag was compared to that calculated in an idealized numerical model of twin air cushions. Indeed for such very low draft planning ship hulls, wavemaking drag is the main hydrodynamic resistance component, which essentially corresponds to the integrated cushion pressure force acting on the sloping free surface $\eta(x, y)$ within the air cushions. For high speed sealift and hence high pressure in the cushions, free surface shape may become quite steep within the cushions and no longer be approximated by linear wave theory.

To simulate this problem, Sung and Grilli[44–46] modified the 3D-FNPF NWT detailed in this paper, by expressing time updating equations in a coordinate system (x', y, z) moving with the ship/cushion velocity $U(t)$, in the x direction. A side effect of this method is that the MEL updating will gradually transport free surface nodes downstream, at a mean velocity U. Hence, a variety of free-surface updating schemes were tested, that allowed for pseudo-Lagrangian updating of free surface nodes, allowing these to keep a fixed x location. Specifically, in this application, the potential is expressed as (more details can be found in the references),

$$\phi(\boldsymbol{x}, t) = Ux + \varphi(\boldsymbol{x}, t) \quad \text{with} \quad x' = x + \int_0^t U(\tau)\mathrm{d}\tau \qquad (4.1)$$
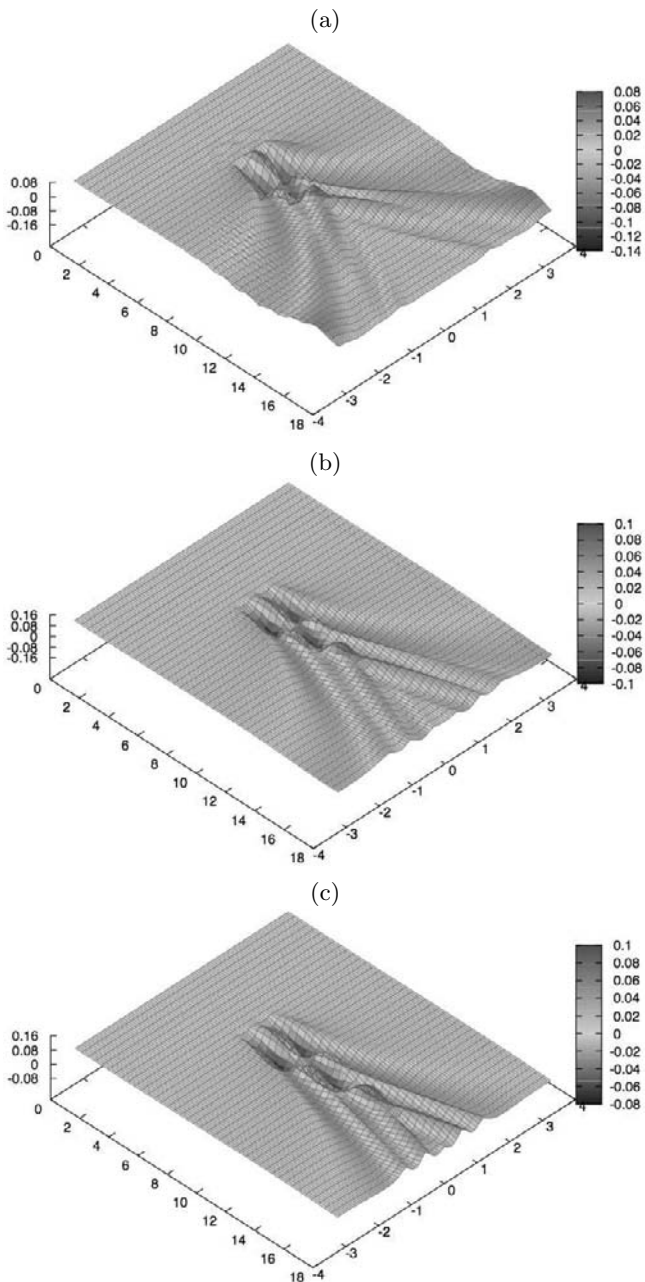
(a)

(b)

(c)

Fig. 15.   Computed free surface elevations for waves generated by twin air cushions moving at speed $U =$ (a) 4, (b) 6, and (c) 8 m/s, with displacement $W = 445$ N. Quasi-steady state is established after 300 time steps (for $t = 18$, 12, and 9 s, respectively).[Note, dimensions are made nondimensional using cushion half-length $a = 0.745$.]

and the pseudo-Lagrangian operator is,

$$\frac{\tilde{\text{D}}}{\text{D}t} = \frac{\partial}{\partial t} + \frac{\partial \varphi}{\partial y}\frac{\partial}{\partial y} + \left\{\frac{\partial \varphi}{\partial t} + \frac{\partial \eta}{\partial x}(U - \frac{\partial \varphi}{\partial x})\right\}\frac{\partial}{\partial z}. \qquad (4.2)$$

Another problem when using such relative axes is that, at the upstream edge of the NWT, a fast mean current flows under an essentially flat free surface, which typically causes the appearance of instabilities and high frequency oscillations in the model that must be damped using an absorbing beach. Here, this is done by specifying an artificial pressure over a narrow strip of free surface near the leading edge as, $p_a = -\nu\varphi$.

Although the 3D model is capable of simulating the full surface piercing ship hull, we only specify here the surface disturbance caused by a traveling air cushion. As mentioned, for a high speed SES, wavemaking drag is essentially due to cushion pressure effects. Following Harris and Grilli,[54] we perform simulations at model scale, for waves generated by a twin air cushion moving at speed U =4, 6, or 8 m/s in the x direction. A free surface pressure $p_a(x, y)$ is specified in the model (in Eq. (2.5)) over cushions of length $2a = 1.49$ m, width 0.23 m, and total surface area $S_c = 0.685$ m^2. The cushions are set one width apart and their initial x-location is 4.95 m (down from the tank leading edge), in a tank 13.4 m long, 2.3 m wide (10 cushion widths), and 7 m deep (corresponding to the actual experimental towing tank depth). The pressure distribution over the cushions is similar to that used earlier,[44,45] i.e., a double 'tanh' shape in x and y directions, with falloff parameters $\alpha = 5$ and $\beta = 10$. We assume a total displacement of $W = 445$ N for the modeled vehicle and hence an average pressure needed to support this displacement of $p_o = W/S_c = 649$ N/m^2. An absorbing boundary (snake wavemaker) condition is specified in the NWT downstream of the cushions, and no flow conditions on the side walls. We use 81, 45 and 25 nodes in the (x', y, z) directions, respectively. [Note, due to symmetry, only half the domain is represented in the y direction.] For a total of $N_\Gamma = 14{,}946$ nodes, the CPU time per time step, using the FMA-GMRES method is about 4.5 min on a 2 GHz x8664 single processor with 3Gb of RAM (i.e., a total of 1350 min; one of two processors on a Microways 4-bipro node cluster). In separate but similar applications, Sung and Grilli[46] reported a $\sim N_\Gamma^{1.32}$ growth of CPU time, using the FMA-GMRES method on a single processor computer. [Note, these computations included the set-up time of the BEM system matrices, which normally grows as N_Γ^2.]
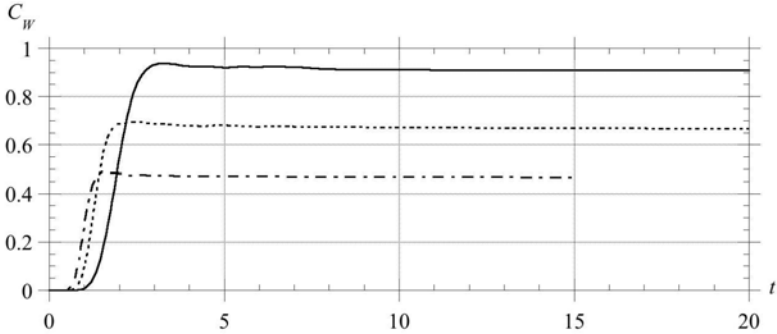
Fig. 16.   Wave resistance coefficient as a function of time, for each test case in Fig. 15: (a) (—); (b) (- - -); (c) (— - —).

After a smooth ramp-up of both cushion speed and pressure over 40 time steps, the model reaches a quasi-steady free surface elevation (Fig. 15) and resistance coefficient value (Fig. 16),

$$C_W = \frac{\rho g a}{W p_0} \int_{S_c} p \frac{\partial \eta}{\partial x} \mathrm{d}S \,. \tag{4.3}$$

Figure 15 shows free surfaces computed after 300 time steps, for the 3 cushion speeds, which all appear in a form similar to the classic Kelvin wave pattern. [Note, because of the finite depth, changes in patch velocity induce changes in the angle of the Kelvin wake.] Figure 16 indicates that the total wave drag coefficients reach stable values in the 3 test cases. Harris and Grilli[54] show that these values agree quite well with experimental measurements, particularly for the two highest speeds (for which the proportion of frictional drag in the experiments is very small).

5. Conclusions

We report on the development, validation, and application of an accurate and versatile model solving FNPF theory with a free surface, using both a higher-order BEM and MEL explicit free surface time updating, in a 3D domain of arbitrary geometry. Various boundary conditions can be specified to generate or absorb waves, such as complex snake wavemakers, actively absorbing boundaries, absorbing beaches, or moving underwater or free surface bodies. In particular, the model is well-suited to simulate wave interactions with surface-piercing moving bodies and the complex

problems occurring in corners and edges, particularly with respect to well-posed boundary conditions and accurate numerical integrations. Although the model yields theoretically fully-populated system matrices, a sparse structure with improved performance can be achieved through using an efficient FMA, combined with the iterative solver GMRES. Recent computations on a single processor computer show a numerical complexity approaching a linear growth with mesh size, beyond some minimum number of nodes.

It should be stressed that our approach, is probably unique and differs in aim from that of more recent faster FNPF solvers that have been implemented to simulate complex sea states over large areas but are limited to non-breaking waves and/or use space periodic domains, and often approximate the FNPF problem to some extent, thus limiting the wave non-linearity that can be achieved (e.g., Refs. 30–33). Here, we sacrifice some potential gain in computational efficiency by implementing a very accurate method in both surface description (including higher-order inter-element continuity), MEL time updating, and costly numerical BEM integrations, that allow to accurately model overturning waves and their properties up to very close to the impact of breaking jets on the free surface, as shown in applications presented in this paper. Such results have been repeatedly shown to approach measurements in precision experiments, to within a surprising degree of accuracy. Another advantage of the present model is its easiness and versatility to simulate complex boundary condition and moving boundaries (both bottom and lateral), including those on surface piercing bodies. An additional advantage of our approach is the capability of validating simpler models and finding their range of validity.

Although the model is not capable of describing wave motion beyond the impact of the plunging jet on the free surface (which terminates computations), its results can be (and have been) used to accurately initialize wave kinematics and pressure close to the breaking point in numerical models solving full NS equations (e.g., using a volume of fluid (VOF) method for the interface reconstruction and tracking). Usually, NS models are computationally very costly (particularly in 3D) and suffer from numerical diffusion, leading to artificial loss of energy over long distances of wave propagation and hence limiting them to fairly small spatial extension. Provided they are properly initialized, such NS models can nevertheless realistically simulate the splash-up phenomenon, as reported in studies of 2D breaking waves using Reynolds averaged NS equations with a k–ϵ turbulent transport equation,[9] and using direct NS simulations,[10] or 3D

breaking waves using a NS model with LES of the turbulent fields.[11,12] A promising development seems to be the actual coupling of BEM-FNPF and VOF-NS models, for pre- and post-breaking waves respectively. This was, e.g., done for 2D[13,14] and 3D[52] problems; the latter work simulated the breaking and post-breaking of solitary waves on a sloping ridge. Similarly, Corte and Grilli[74] initialized a 3D-VOF-NS model with an extreme focused wave, obtained in the 3D-FNPF model as in Ref. 40 or as shown in one of the applications reported in this paper, to calculate extreme wave loads on cylindrical piles of wind mills to be installed in 40-60 m of water in the North and Baltic Seas. The coupling of 3D-FNPF results to other methods such as those based on Smoothed Particle Hydrodynamics (e.g., Ref. 81) would also be an interesting line of work that some scientists have started investigating.

Some of the work reported here is still in progress, such as the FNPF-VOF coupling, the FNPF simulations of wave resistance and dynamic trim angle of various ships, with hulls of complex geometry (with or without an air cushion). In this respect, to be able to sufficiently resolve both the ship hull and the free surface, the image method is being fully integrated with the FMA (in both y and z directions) for the ship generated wave simulations, similar to the latest computations of rogue waves, and the FMA method is being parallelized, using a newly acquired library, to implement it on large computer clusters.

A.1. Detailed Expressions of Laplace's Equation and Accelerations on the Boundary

In the general non-orthogonal curvilinear system $(\boldsymbol{s}, \boldsymbol{m}, \boldsymbol{n})$ on the boundary, with $\kappa = \cos(\boldsymbol{s}, \boldsymbol{m})$, Laplace's equation for the potential reads,

$$
\begin{aligned}
\phi_{nn} = \frac{1}{1-\kappa^2}\Bigg\{ & 2\kappa\phi_{sm} - \phi_{ss} - \phi_{mm} + \frac{\phi_s}{1-\kappa^2}\{(\boldsymbol{x}_{ss} + \boldsymbol{x}_{mm} - 2\kappa\boldsymbol{x}_{sm})\cdot\boldsymbol{s} \\
& - \kappa(\boldsymbol{x}_{ss} + \boldsymbol{x}_{mm} - 2\kappa\boldsymbol{x}_{sm})\cdot\boldsymbol{m}\} - \frac{\phi_m}{1-\kappa^2}\{\kappa(\boldsymbol{x}_{mm} + \boldsymbol{x}_{ss} - 2\kappa\boldsymbol{x}_{sm})\cdot\boldsymbol{s} \\
& - (\boldsymbol{x}_{ss} + \boldsymbol{x}_{mm} - 2\kappa\boldsymbol{x}_{sm})\cdot\boldsymbol{m}\} + \phi_n\{\boldsymbol{x}_{ss} + \boldsymbol{x}_{mm} - 2\kappa\boldsymbol{x}_{sm}\}\cdot\boldsymbol{n}\Bigg\}.
\end{aligned}
$$

(A.1)

Then, substituting Equation (A.1) into the expression for the particle acceleration on the boundary yields,

$$
\frac{\mathrm{D}\boldsymbol{u}}{\mathrm{D}t} = \left(\frac{\partial}{\partial t} + \boldsymbol{\nabla}\phi \cdot \boldsymbol{\nabla} \right) \boldsymbol{\nabla}\phi
$$

$$
= \frac{\boldsymbol{s}}{1-\kappa^2}\Bigg[\phi_{ts} - \kappa\phi_{tm} + \phi_n\phi_{ns} - \kappa\phi_n\phi_{nm} + \frac{1}{1-\kappa^2}\Big\{ \phi_s\phi_{ss} - 2\kappa\phi_s\phi_{sm}
$$

$$
+ \kappa^2\phi_s\phi_{mm} - \kappa\phi_m\phi_{mm} + (1+\kappa^2)\phi_m\phi_{sm} - \kappa\phi_m\phi_{ss} \Big\} + \frac{\phi_s^2}{(1-\kappa^2)^2}
$$

$$
\Big\{ (2\kappa\boldsymbol{x}_{sm} - \boldsymbol{x}_{ss} - \kappa^2\boldsymbol{x}_{mm})\cdot\boldsymbol{s} + \kappa(\boldsymbol{x}_{ss} - 2\kappa\boldsymbol{x}_{sm} + \kappa^2\boldsymbol{x}_{mm})\cdot\boldsymbol{m} \Big\}
$$

$$
+ \frac{\phi_s\phi_m}{(1-\kappa^2)^2}\Big\{ (2\kappa\boldsymbol{x}_{ss} - (1+3\kappa^2)\boldsymbol{x}_{sm} + \kappa(1+\kappa^2)\boldsymbol{x}_{mm})\cdot\boldsymbol{s}
$$

$$
- ((1+\kappa^2)\boldsymbol{x}_{ss} - \kappa(3+\kappa^2)\boldsymbol{x}_{sm} + 2\kappa^2\boldsymbol{x}_{mm})\cdot\boldsymbol{m} \Big\} + \frac{\phi_m^2}{(1-\kappa^2)^2}\Big\{ \kappa
$$

$$
((1+\kappa^2)\boldsymbol{x}_{sm} - \kappa\boldsymbol{x}_{ss} - \kappa\boldsymbol{x}_{mm})\cdot\boldsymbol{s} + (\kappa\boldsymbol{x}_{ss} - (1+\kappa^2)\boldsymbol{x}_{sm} + \kappa\boldsymbol{x}_{mm})
$$

$$
\cdot\boldsymbol{m} \Big\} + \frac{\phi_s\phi_n}{1-\kappa^2}\kappa\Big\{ 2\boldsymbol{x}_{sm} - \kappa\boldsymbol{x}_{ss} - \kappa\boldsymbol{x}_{mm} \Big\}\cdot\boldsymbol{n} + \frac{\phi_m\phi_n}{1-\kappa^2}\Big\{ \kappa\boldsymbol{x}_{ss} -
$$

$$
(1+\kappa^2)\boldsymbol{x}_{sm} + \kappa^3\boldsymbol{x}_{mm} \Big\}\cdot\boldsymbol{n} \Bigg] + \frac{\boldsymbol{m}}{1-\kappa^2}\Bigg[\phi_{tm} - \kappa\phi_{ts} - \kappa\phi_n\phi_{ns} +
$$

$$
\phi_n\phi_{nm} + \frac{1}{1-\kappa^2}\Big\{ (1+\kappa^2)\phi_s\phi_{sm} - \kappa\phi_s\phi_{ss} - \kappa\phi_s\phi_{mm} + \phi_m\phi_{mm} -
$$

$$
2\kappa\phi_m\phi_{sm} + \kappa^2\phi_m\phi_{ss} \Big\} + \frac{\phi_s^2}{(1-\kappa^2)^2}\Big\{ (\kappa\boldsymbol{x}_{ss} - (1+\kappa^2)\boldsymbol{x}_{sm} + \kappa\boldsymbol{x}_{mm})
$$

$$
\cdot\boldsymbol{s} - \kappa(\kappa\boldsymbol{x}_{ss} - (1+\kappa^2)\boldsymbol{x}_{sm} + \kappa\boldsymbol{x}_{mm})\cdot\boldsymbol{m} \Big\} + \frac{\phi_s\phi_m}{(1-\kappa^2)^2}\Big\{ (-2\kappa^2\boldsymbol{x}_{ss} +
$$

$$
\kappa(3+\kappa^2)\boldsymbol{x}_{sm} - (1+\kappa^2)\boldsymbol{x}_{mm})\cdot\boldsymbol{s} + (\kappa(1+\kappa^2)\boldsymbol{x}_{ss} - (1+3\kappa^2)\boldsymbol{x}_{sm} +
$$

$$
2\kappa\boldsymbol{x}_{mm})\cdot\boldsymbol{m} \Big\} + \frac{\phi_m^2}{(1-\kappa^2)^2}\Big\{ \kappa(\kappa^2\boldsymbol{x}_{ss} - 2\kappa\boldsymbol{x}_{sm} + \boldsymbol{x}_{mm}\cdot\boldsymbol{s})\cdot\boldsymbol{s} +
$$

$$
(2\kappa\boldsymbol{x}_{sm} - \kappa^2\boldsymbol{x}_{ss} - \boldsymbol{x}_{mm})\cdot\boldsymbol{m} \Big\} + \frac{\phi_s\phi_n}{1-\kappa^2}\Big\{ (\kappa^3\boldsymbol{x}_{ss} - (1+\kappa^2)\boldsymbol{x}_{sm} +
$$

$$
\kappa\boldsymbol{x}_{mm})\cdot\boldsymbol{n} \Big\} + \frac{\phi_m\phi_n}{1-\kappa^2}\Big\{ \kappa(2\boldsymbol{x}_{sm} - \kappa\boldsymbol{x}_{ss} - \kappa\boldsymbol{x}_{mm})\cdot\boldsymbol{n} \Big\} \Bigg] + \frac{\boldsymbol{n}}{1-\kappa^2}
$$

$$
\Bigg[(1-\kappa^2)\phi_{tn} + \phi_s\phi_{ns} - \kappa\phi_s\phi_{nm} - \kappa\phi_m\phi_{ns} + \phi_m\phi_{nm} - \phi_n\phi_{ss} +
$$

$$
2\kappa\phi_n\phi_{sm} - \phi_n\phi_{mm} + \frac{\phi_s^2}{1-\kappa^2}\Big\{ (\boldsymbol{x}_{ss} - 2\kappa\boldsymbol{x}_{sm} + \kappa^2\boldsymbol{x}_{mm})\cdot\boldsymbol{n} \Big\} +
$$

$$\frac{2\phi_s\phi_m}{1-\kappa^2}\Big\{\big((1+\kappa^2)\boldsymbol{x}_{sm} - \kappa\boldsymbol{x}_{ss} - \kappa\boldsymbol{x}_{mm}\big)\cdot\boldsymbol{n}\Big\} + \frac{\phi_m^2}{1-\kappa^2}\Big\{(\kappa^2\boldsymbol{x}_{ss} -$$

$$2\kappa\boldsymbol{x}_{sm} + \boldsymbol{x}_{mm})\cdot\boldsymbol{n}\Big\} + \frac{\phi_s\phi_n}{1-\kappa^2}\Big\{(\boldsymbol{x}_{ss} - 2\kappa\boldsymbol{x}_{sm} + \boldsymbol{x}_{mm})\cdot\boldsymbol{s} + \kappa(2\kappa\boldsymbol{x}_{sm}$$

$$-\boldsymbol{x}_{ss} - \boldsymbol{x}_{mm})\cdot\boldsymbol{m}\Big\} + \frac{\phi_m\phi_n}{1-\kappa^2}\Big\{\kappa(2\kappa\boldsymbol{x}_{sm} - \boldsymbol{x}_{ss} - \boldsymbol{x}_{mm})\cdot\boldsymbol{s} + (\boldsymbol{x}_{ss}$$

$$-2\kappa\boldsymbol{x}_{sm} + \boldsymbol{x}_{mm})\cdot\boldsymbol{m}\Big\} + \phi_n^2\Big\{(\boldsymbol{x}_{ss} - 2\kappa\boldsymbol{x}_{sm} + \boldsymbol{x}_{mm})\cdot\boldsymbol{n}\Big\}\Big]. \quad\text{(A.2)}$$

For $\kappa = 0$, the orthogonal case, Eqs. (2.24), (A.1) and (A.2) simplify to the expressions given in[36] (Equations (60), (61) and (62)). Note that, when $\boldsymbol{s}\cdot\boldsymbol{m} = 0$, one has the identities $\boldsymbol{x}_{ss}\cdot\boldsymbol{m} = -\boldsymbol{x}_{sm}\cdot\boldsymbol{s}$ and $\boldsymbol{x}_{sm}\cdot\boldsymbol{m} = -\boldsymbol{x}_{mm}\cdot\boldsymbol{s}$.

References

1. Peregrine, D. H. (1983). Breaking waves on beaches. *Ann. Rev. Fluid Mech.*, **15**, 149–178.
2. Banner, M. L. and Peregrine, D. H. (1993). Breaking waves in deep water. *Ann. Rev. Fluid Mech.*, **25**, 373–397.
3. Dommermuth, D. G., Yue, D. K. P., Lin, W. M., Rapp, R. J., Chan, E. S. and Melville, W. K. (1988). Deep-water plunging breakers: a comparison between potential theory and experiments. *J. Fluid Mech.*, **189**, 423–442.
4. Skyner, D. J. (1996). A comparison of numerical predictions and experimental measurements of the internal kinematics of a deep-water plunging wave. *J. Fluid Mech.*, **315**, 51–64.
5. Grilli, S. T., Subramanya, R., Svendsen, I. A. and Veeramony, J. (1994). Shoaling of solitary waves on plane beaches. *J. Waterway, Port, Coastal, Ocean Engng*, **120**, 609–628.
6. Grilli, S. T., Svendsen, I. A. and Subramanya, R. (1997). Breaking criterion and characteristics for solitary waves on slopes. *J. Waterway, Port, Coastal, Ocean Engng*, **123**(3), 102–112.
7. Grilli, S. T., Svendsen, I. A. and Subramanya, R. (1998). Closure of: Breaking Criterion and Characteristics for Solitary Waves on Slopes. *J. Waterway, Port, Coastal, Ocean Engng*, **124**(6), 333–335.
8. Grilli, S. T., Gilbert, R., Lubin, P., Vincent, S., Legendre, D., Duvam, M., Kimmoun, O., Branger, H., Devrard, D., Fraunie, P., Abadie, S. (2004). Numerical modeling and experiments for solitary wave shoaling and breaking over a sloping beach. In *Proc. 14th Offshore and Polar Engng. Conf.* (ISOPE04, Toulon, France, May 2004), 306–312.
9. Lin, P. and Liu, P. L.-F. (1998). A numerical study of breaking waves in the surf zone. *J. Fluid Mech.*, **359**, 239–264.

10. Chen, G., Kharif, C., Zaleski, S. and Li, J. (1999). Two-dimensional Navier–Stokes simulation of breaking waves. *Phys. Fluids*, **11**, 121–133.

11. Christensen, E. D. and Deigaard, R. (2001). Large eddy simulation of breaking waves. *Coastal Engng.*, **42**, 53–86.

12. Lubin, P. (2004). *Large Eddy Simulations of Plunging Breaking Waves.* Ph.D Dissertation, University of Bordeaux I, France.

13. Guignard, S., Grilli, S. T., Marcer, R. and Rey, V. (1999). Computation of shoaling and breaking waves in nearshore areas by the coupling of BEM and VOF methods. In *Proc. 9th Intl Offshore and Polar Engng Conf.* (Brest, France), 304–309, ISOPE.

14. Lachaume, C., Biausser, B., Grilli, S. T., Fraunie, P. and Guignard, S. (2003). Modeling of breaking and post-breaking waves on slopes by coupling of BEM and VOF methods. In *Proc. 13th Intl Offshore and Polar Engng Conf.* (Honolulu, USA), 353–359, ISOPE.

15. Longuet-Higgins, M. S. and Cokelet, E. D. (1976). The deformation of steep surface waves on water. I. A numerical method of computation. *Proc. R. Soc. Lond.*, A **350**, 1–26.

16. Vinje, T. and Brevig, P. (1981). Numerical simulation of breaking waves. *Adv. Water Resour.*, **4**, 77–82.

17. Baker, G. R., Meiron, D. I. and Orszag, S. A. (1982). Generalized vortex methods for free-surface flow problems. *J. Fluid Mech.*, **123**, 477–501.

18. New, A. L. (1983). A class of elliptical free-surface flows. *J. Fluid Mech.*, **130**, 219–239.

19. New, A. L., McIver, P. and Peregrine, D. H. (1985). Computations of overturning waves. *J. Fluid Mech.*, **150**, 233–251.

20. Grilli, S. T., Skourup, J. and Svendsen, I. A. (1989). An Efficient Boundary Element Method for Nonlinear Water Waves. *Engng. Anal. Bound. Elem.*, **6**(2), 97–107.

21. Cointe, R. (1990). Numerical simulation of a wave channel. *Engng Anal. Bound. Elem.*, **7**, 167–177.

22. Grilli, S. T. and Subramanya, R. (1996). Numerical modelling of wave breaking induced by fixed or moving boundaries. *Comput. Mech.*, **17**, 374–391.

23. Grilli, S. T. and Horrillo, J. (1997). Numerical generation and absorption of fully nonlinear periodic waves. *J. Engng Mech.*, **123**, 1060–1069.

24. Romate, J. E. (1989). *The Numerical Simulation of Nonlinear Gravity Waves in Three Dimensions using a Higher Order Panel Method.* Ph.D. Dissertation. Department of Applied Mathematics, University of Twente, The Netherland, 1989.

25. Boo, S. Y., Kim, C. H. and Kim, M. H. (1994). A numerical wave tank for nonlinear irregular waves by three-dimensional higher-order boundary element method. *Intl J. Offshore and Polar Engng*, **4**(4), 265–272.

26. Broeze, J. (1993). Numerical modelling of nonlinear free surface waves with a three-dimensional panel method. PhD thesis, University of Twente, Enschede, The Netherlands.

27. Broeze, J., Van Daalen, E. F. G. and Zandbergen, P. J. (1993). A three-dimensional panel method for nonlinear free surface waves on vector computers. *Comput. Mech.*, **13**, 12–28.

28. Ferrant, P. (1996). Simulation of strongly nonlinear wave generation and wave–body interactions using a fully nonlinear MEL model. In *Proc. 21st Symp. on Naval Hydrodynamics*, Trondheim, Norway, pp. 93–108.

29. Celebi, M. S., Kim, M. H. and Beck, R. F. (1998). Fully nonlinear three-dimensional numerical wave tank simulations. *J. Ship. Res.*, **42**, 33–45.

30. Bonnefoy, F., Le Touze, D. and Ferrant, P. (2004). Generation of fully-nonlinear prescribed wave fields using a high-order spectral method, In *Proc. 14th Offshore and Polar Engng. Conf.* (ISOPE 2004, Toulon, France), 257–263, 2004.

31. Clamond, D., Fructus, D., Grue, J. and Kristiansen, O. (2005). An efficient model for three-dimensional surface wave simulations. Part II: Generation and absorption. *J. Comput. Phys.*, **205**, 686–705.

32. Fructus, D., Clamond, D., Grue, J. and Kristiansen, O. (2005). An efficient model for three-dimensional surface wave simulations. Part I: Free space problems. *J. Comput. Phys.*, **205**, 665–685.

33. Ducrozet, G., Bonnefoy, F., Le Touzé, D. and Ferrant, P. (2007). 3-D HOS simulations of extreme waves in open seas. *Nat. Hazards Earth Syst. Sci.*, **7**, 109–122.

34. Xü, H. and Yue, D. K. P. (1992). Computations of fully nonlinear three-dimensional water waves. In *Proc. 19th Symp. on Naval Hydrodynamics* (Seoul, Korea).

35. Xue, M., Xü, H., Liu, Y. and Yue, D. K. P. (2001). Computations of fully nonlinear three-dimensional wave–wave and wave–body interactions. Part 1. Dynamics of steep three-dimensional waves. *J. Fluid Mech.*, **438**, 11–39.

36. Grilli, S. T., Guyenne, P. and Dias, F. (2001). A fully nonlinear model for three-dimensional overturning waves over an arbitrary bottom. *Intl J. Numer. Meth. Fluids*, **35**, 829–867.

37. Guyenne, P., Grilli, S. T. and Dias, F. (2000). Numerical modelling of fully nonlinear three-dimensional overturning waves over arbitrary bottom. In *Proc. 27th Intl Conf. on Coastal Engng* (Sydney, Australia), 417–428, ASCE.

38. Brandini, C. and Grilli, S. T. (2001a). Modeling of freak wave generation in a three-dimensional NWT. In *Proc. 11th Intl Offshore and Polar Engng Conf.*, Stavanger, Norway, pp. 124–131, ISOPE.

39. Brandini, C. and Grilli, S. T. (2001b). Three-dimensional wave focusing in fully nonlinear wave models. In *Proc. 4th Intl Symp. on Ocean Wave Measurement and Analysis* (San Francisco, USA), 1102–1111, ASCE.

40. Fochesato, C., Grilli, S. T. and Dias, F. (2007). Numerical modeling of extreme rogue waves generated by directional energy focusing. *Wave Motion*, **44**, 395–416.

41. Grilli, S. T., Vogelmann, S. and Watts, P. (2002). Development of a three-dimensional numerical wave tank for modelling tsunami generation by underwater landslides. *Engng Anal. Bound. Elem.*, **26**, 301–313.

42. Enet, F. (2006). *Tsunami generation by underwater landslides*. Ph.D Dissertation, Department of Ocean Engineering, University of Rhode Island.

43. Enet, F. and Grilli, S. T. (2005). Tsunami Landslide Generation: Modelling and Experiments. In *Proc. 5th Intl. n Ocean Wave Measurement and Analysis* (WAVES 2005, Madrid, Spain, July 2005), IAHR Pub., paper 88, 10 pp.

44. Sung, H. G. and Grilli, S. T., (2005). Numerical Modeling of Nonlinear Surface Waves caused by Surface Effect Ships. Dynamics and Kinematics. In *Proc. 15th Offshore and Polar Engng. Conf.* (ISOPE05, Seoul, South Korea, June 2005), 124–131.

45. Sung, H. G. and Grilli, S. T. (2006). Combined Eulerian-Lagrangian or Pseudo-Lagrangian, Descriptions of Waves Caused by an Advancing Free Surface Disturbance. In *Proc. 16th Offshore and Polar Engng. Conf.* (ISOPE06, San Francisco, California, June 2006), 487–494.

46. Sung, H. G. and Grilli, S. T. (2008). BEM Computations of 3D Fully Nonlinear Free Surface Flows Caused by Advancing Surface Disturbances. *Intl. J. Offshore and Polar Engng.*, **18**(4), 292–301.

47. Kervella, Y., Dutykh, D. and Dias, F. (2007). Comparison between three-dimensional linear and nonlinear tsunami generation models. *Theoretical and Computational Fluid Dynamics*, **21**, 245–269.

48. Tong, R. P. (1997) A new approach to modelling an unsteady free surface in boundary integral methods with application to bubble–structure interactions. *Math. Comput. Simul.*, **44**, 415–426.

49. Fochesato, C. and Dias, F. (2006). A fast method for nonlinear three-dimensional free-surface waves, *Proc. Roy. Soc. Lond. A*, **462**, 2715–2735.

50. Fochesato, C., Grilli, S. T. and Guyenne, P. (2005). Note on non-orthogonality of local curvilinear coordinates in a three-dimensional boundary element method. *Intl J. Numer. Meth. Fluids*, **48**, 305–324.

51. Tanaka, M. (1986). The stability of solitary waves. *Phys. Fluids*, **29**, 650–655.

52. Biausser, B., Grilli, S. T., Fraunie, P. and Marcer, R. (2004). Numerical analysis of the internal kinematics and dynamics of 3D breaking waves on slopes. *Intl J. Offshore and Polar Engng*, **14**, 247–256.

53. Guyenne, P. and Grilli, S. T. (2006). Numerical study of three-dimensional overturning waves in shallow water. *J. Fluid Mech.*, **547**, 361–388.

54. Harris, J. C., and Grilli, S. T. (2007). Computation of the wavemaking resistance of a Harley surface effect ship. In *Proc. 17th Offshore and Polar Engng. Conf.* (ISOPE07, Lisbon, Portugal, July 2007), 3732–3739.

55. Grilli, S. T., Voropayev, S., Testik, F. Y. and Fernando, H. J. S. (2003). Numerical Modeling and Experiments of Wave Shoaling over Buried Cylinders in Sandy Bottom. In *Proc. 13th Offshore and Polar Engng. Conf.* (ISOPE03, Honolulu, USA, May 2003), 405–412.

56. Dias, F., Dyachenko, A. and Zakharov, V. (2008) Theory of weakly damped free-surface flows: a new formulation based on potential flow solutions. *Physics Letters A* **372**, 1297–1302.

57. Dias, F. and Bridges, T. (2006). The numerical computation of freely propagating time-dependent irrotational water waves, *Fluid Dyn. Research*, **38**, 803–830.

58. Grilli, S. T. (1985). Experimental and Numerical Study of the Hydrodynamic Behavior of Large Self-propelled Floating Gates for Maritime Locks and Tidal-surge Barriers. Collection des Publications de la Faculté des Sciences Appliquées de l'Université de Liège, No. **99**, 447 pps, Liège, Belgium.

59. Grilli, S. T. and Svendsen, I. A. (1990). Corner Problems and Global Accuracy in the Boundary Element Solution of Nonlinear Wave Flows. *Engng. Analysis Boundary Elemt.*, **7**(4), 178–195.

60. Grilli, S. T. and Subramanya, R. (1994). Quasi-singular integrals in the modelling of nonlinear water waves in shallow water. *Engng Anal. Bound. Elem.*, **13**, 181–191.

61. Brebbia, C. A. (1978). *The Boundary Element Method for Engineers*. John Wiley and Sons.

62. Badmus, T., Cheng, A. H.-D. and Grilli, S. T. (1993). A three-dimensional Laplace transform BEM for poroelasticity. *Intl. Numer. Meth. Engng.*, **36**, 67–85.

63. Greengard, L. and Rokhlin, V. (1987). A fast algorithm for particle simulations. *J. Comput. Phys.*, **73**, 325–348.

64. Rokhlin, V. (1985). Rapid solution of integral equations of classical potential theory. *J. Comput. Phys.* **60**, 187–207.

65. Nishimura, N. (2002). Fast multipole accelerated boundary integral equation methods. *Appl. Mech. Rev.*, **55**, 299–324.

66. Korsmeyer, F. T., Yue, D. K. P. and Nabors, K. (1993). Multipole-Accelerated Preconditioned Iterative Methods for Three-Dimensional Potential Problems. Presented at *15th Intl. Conf. on Boundary Element*, Worcester, MA.

67. Scorpio, S. and Beck, F. (1996). A Multipole Accelerated Desingularized Method for Computing Nonlinear Wave Forces on Bodies. Presented at *15th Intl. Conf. Offshore Mech. Arctic Engng.* (Florence, Italy).

68. Graziani, G. and Landrini, M. (1999). Application of multipoles expansion technique to two-dimensional nonlinear free-surface flows. *J. Ship Research*, **43**, 1–12.

69. Srisupattarawanit, T., Niekamp, R. and Matthies, H. G. (2006). Simulation of nonlinear random finite depth waves coupled with an elastic structure. *Comput. Methods Appl. Mech. Engrg.*, **195**, 3072–3086.

70. Fochesato, C. (2004). *Modèles numériques pour les vagues et les ondes internes*. Ph.D Dissertation, Centre de Mathématiques et de Leurs Applications. Ecole Normale Supérieure de Cachan.

71. Greengard, L. (1988). *The Rapid Evaluation of Potential Fields in Particle Systems,* MIT Press, Cambridge, MA, 1988.

72. Dalrymple, R. A. (1989). Directional wavemaker theory with sidewall reflection, *J. Hydraulic Res.*, **27**(1), 23–34.

73. Kharif, C. and Pelinovsky, E. (2003). Physical mechanisms of the rogue wave phenomenon, *Eur. J. Mech. B/Fluids*, **22**, 603–634.

74. Corte, C. and Grilli, S. T. (2006). Numerical Modeling of Extreme Wave Slamming on Cylindrical Offshore Support Structures. In *Proc. 16th Offshore and Polar Engng. Conf.* (ISOPE06, San Francisco, CA, June 2006), 394–401.

75. Tappin, D. R., Watts, P. and Grilli, S. T. (2008). The Papua New Guinea tsunami of 1998: anatomy of a catastrophic event, *Nat. Hazards Earth Syst. Sci.*, **8**, 243–266, www.nat-hazards-earth-syst-sci.net/8/243/2008/.

76. Grilli, S. T. and Watts, P. (1999). Modeling of waves generated by a moving submerged body. Applications to underwater landslides. *Engng. Analysis Boundary Elemt.*, **23**, 645–656.

77. Grilli, S. T. and Watts, P. (2005). Tsunami generation by submarine mass failure Part I: Modeling, experimental validation, and sensitivity analysis. *J. Waterway Port Coastal and Ocean Engng.*, **131**(6), 283–297.

78. Watts, P., Grilli, S. T., Tappin, D. and Fryer, G. J. (2005). Tsunami generation by submarine mass failure Part II: Predictive Equations and case studies. *J. Waterway Port Coastal and Ocean Engng.*, **131**(6), 298–310.

79. Watts, P., Grilli, S. T., Kirby, J. T., Fryer, G. J. and Tappin, D. R. (2003). Landslide tsunami case studies using a Boussinesq model and a fully nonlinear tsunami generation model. *Natural Hazards and Earth Syst. Sc.*, **3**, 391–402.

80. Enet, F. and Grilli, S. T. (2007). Experimental Study of Tsunami Generation by Three-dimensional Rigid Underwater Landslides. *J. Waterway Port Coastal and Ocean Engng.*, **133**(6), 442–454.

81. Dalrymple, R. A. and Rogers, B. D. (2006). Numerical Modeling of Water Waves with the SPH Method. *Coastal Engineering*, **53**(2–3), 141–147.